A transparent constrained stochastic framework for urban expansion forecasting and future service-network screening

Cape Town demonstration using annual building evidence, empirical land constraints, spatial hindcasting, and multi-horizon ensembles

Jaco Moolman
Independent Researcher, Cape Town, South Africa
Corresponding author: jacomoolman1890@gmail.com
ORCID: https://orcid.org/0009-0004-3463-9803
Web: https://jacomoolman.co.za
Article type: Research Article
Date of this working version: 7 September 2026 (version 6)

Cover sheet. The manuscript begins on the following page.

A transparent constrained stochastic framework for urban expansion forecasting and future service-network screening

Cape Town demonstration using annual building evidence, empirical land constraints, spatial hindcasting, and multi-horizon ensembles

Abstract

Spatial forecasts of urban expansion require separate, auditable answers to two questions: how much built area is assumed to appear, and where it is allocated. This study presents a constrained stochastic workflow and demonstrates it for metropolitan Cape Town, South Africa. Annual Open Buildings Temporal building-presence surfaces for 2016–2023 are harmonised to a 10 m grid and cleaned with a temporal median and a suffix-persistence rule. A binned logistic model ranks unbuilt cells on distance to the built edge, local and neighbourhood built fractions, and direct adjacency, with the distance and neighbourhood curves projected onto monotone ones after fitting. Terrain, flood and water enter as a separate multiplier rather than inside that fit, and a weak directional term and a detached-growth pool modify the allocation. Demand is supplied independently of location potential, and weighted sampling without replacement updates the urban state at every step across twelve replicates.

A spatially blocked classifier diagnostic returned ROC-AUC 0.880 and PR-AUC 0.307; its best-threshold F1 of 0.456 is optimistic, because that threshold was chosen on the same held-out cells. The end-to-end 2016–2023 hindcast, supplied with observed annual quantities, achieved a 29.02% pixel hit rate and 16.97% Figure of Merit, 7.9 times the uniform-random value. It is an in-period reconstruction rather than an independent forecast test, because location, direction, detached share and terrain strength are all calibrated on the interval it is scored over. The hindcast reproduced dominant edge expansion, overpredicted infill, almost eliminated fringe growth, and missed the observed north-easterly growth bearing by about 35°. The aggregate hit rate also conceals a strong asymmetry: recall falls from 39.2% for change immediately adjacent to the built edge to under 1% beyond about 40 m, and from 36.6% for change in patches under 0.1 ha to 0.9% for patches larger than 50 ha, so the workflow reproduces incremental thickening of an existing perimeter and not the appearance of new districts. Under the central scenario, new built area after a modelled 2026 baseline is 54.9 km² by 2036, 249.7 km² by 2076 and 441.3 km² by 2126. A downstream screen combines forecast growth pressure, straight-line distance from an existing bank network, and developability to rank neighbourhood-scale ATM and branch opportunities. All of these are conditional scenarios and screening hypotheses, not parcel, timing, demographic, or investment predictions.

Keywords: urban growth; land-change modelling; cellular automata; stochastic allocation; spatial hindcasting; ensemble forecast; service accessibility; Cape Town

1. Introduction

Urban expansion models translate evidence about past land change into conditional statements about possible futures. Cellular-automata approaches have long represented local neighbourhood interaction, constraints, stochasticity, and feedback between a changing urban state and its next transition [7,8]. Later land-change frameworks emphasised the need to distinguish demand from spatial allocation, represent cross-scale drivers, and make scenario assumptions explicit [9]. Patch-generating methods have also shown why detached seeds and patch morphology cannot always be recovered by cell-by-cell suitability alone [10]. These ideas are scientifically useful only when calibration, validation, and uncertainty are reported honestly [11].

Three recurrent problems motivate the present workflow. First, an annual remote-sensing product can flicker even when the underlying building stock is persistent. Second, physical constraints and urban-pattern predictors can be counted twice if they are hidden in one fitted score. Third, a single deterministic map can imply a level of site precision that neither the observations nor the model support. Validation also has several meanings. A held-out classifier diagnostic evaluates the ranking model, whereas an end-to-end hindcast evaluates the complete iterative allocator. Supplying the observed quantity to a hindcast tests allocation, not future demand. Figure of Merit is useful for change maps because it ignores the large number of correctly unchanged cells [12], but no one metric captures quantity, allocation, morphology, and uncertainty [11–13].

This paper develops an auditable chain from annual building evidence to future scenarios and then to a separate service-network screen. Cape Town is a demonstration case, not evidence that the fitted numerical parameters transfer unchanged. The reusable contribution is the separation of observation cleaning, empirical physical constraints, dynamic urban-pattern ranking, independent demand, stochastic allocation, ensemble interpretation, and downstream screening. The paper asks:

1. How can annual building evidence be converted into a stable transition history without disguising observation uncertainty?
2. How can terrain, flood, water, urban continuity, direction, and detached growth be combined while keeping their roles visible?
3. What does the model reproduce in a 2016–2023 hindcast, and which spatial errors remain?
4. How do scenario totals and exact-cell ensemble agreement change from 2036 to 2126?
5. How can the forecast support neighbourhood-scale service screening without being misrepresented as a site-selection model?

2. Study area and source evidence

2.1 Spatial frame and analysis scale

The common analysis frame is EPSG:32734 (WGS 84 / UTM zone 34S), 7168 × 7168 cells, 10 m per cell, and 71.68 km per side. It covers metropolitan Cape Town, the Cape Flats, northern growth corridors, the Atlantic and False Bay coasts, and the Somerset West–Strand edge. The 10 m grid is an analysis and allocation grid; it is not a claim that the source imagery directly resolves individual 10 m parcels.

Open Buildings 2.5D Temporal provides annual building presence, fractional count, and height surfaces for 2016–2023 from Sentinel-2 image stacks [1,16]. Google reports an effective source resolution of approximately 4 m, while distributed rasters have a finer nominal pixel spacing. The present workflow resamples the building-presence surface to the common 10 m grid. Figure 1 shows both the metropolitan pattern and the grid scale used by the model.

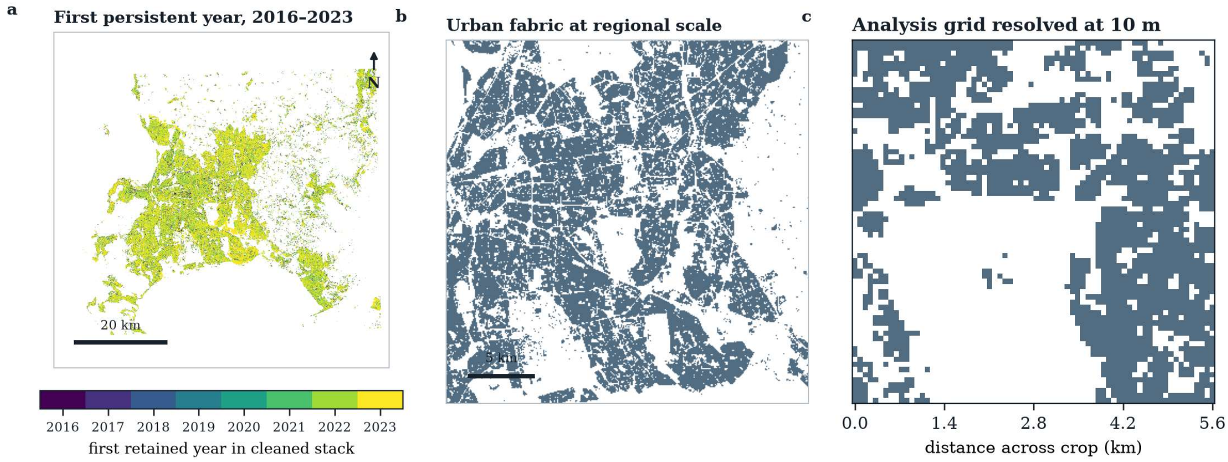

Figure 1. Annual building evidence and analysis scale. (a) First year in which a cell remains present after temporal cleaning, over the full 71.68 km frame. (b) Regional urban fabric. (c) A local crop showing the 10 m analysis cells after aggregation for display. All map panels in this paper share the same north-up EPSG:32734 frame and orientation. Colours in panel (a) indicate retained observation timing, not verified construction dates.

2.2 Historical and environmental sources

The Global Human Settlement Layer (GHSL) built-surface product provides 1975–2020 long-run context and the low-growth scenario [2]. JRC Global Surface Water supplies the hard water exclusion [3]. Copernicus DEM GLO-30 underlies the aligned relief render [4]. The archived acquisition workflow also includes JRC Global River Flood Hazard and MERIT Hydro layers [5,6]. The production forecast consumed aligned renders rather than physical slope degrees or raw flood depths. Consequently, terrain luminance and flood-render intensity are empirical model inputs; no result is interpreted as a universal slope or water-depth threshold. The same qualification applies to the water mask: a cell is treated as water where the water-occurrence render reaches a luminance of 60 or more. That threshold places 0.13% of the 2023 built mask inside water, which is the expected coastal-edge residue of a 30 m source resampled to 10 m. Table 1 summarises each source and the qualification that travels with it.

Table 1. Source evidence and its limits. Every entry is a public product or an author-compiled snapshot; none is a cadastral or survey record, and the qualifications in the third column bound what any downstream result can mean.

Evidence	Role in this study	Important qualification
Open Buildings Temporal, 2016–2023	annual observed states; transition labels; raw area trend	model-derived building presence, not cadastral construction dates
GHSL built surface, 1975–2020	long-run context; low demand scenario	different product and temporal support from Open Buildings
Copernicus DEM-derived render	terrain response and developability	render luminance, not slope in degrees
Flood render and water occurrence	soft flood penalty; hard water exclusion	flood penalty is not a return-period risk model
Facility snapshot, 2 August 2026	current ATM and branch service points	author-compiled operational snapshot; rights require final review

2.3 Current facility network

The downstream demonstration uses an author-compiled 2 August 2026 snapshot of 447 facilities: 357 ATMs and 90 branches. For cash-access screening, branches and ATMs both count as existing service. For branch screening, only the 90 branches count. This dataset is not used to fit or modify the urban forecast.

3. Methods

3.1 Binary observation and temporal persistence

For cell i and observation year t, a fixed threshold $\tau = 0.16$ converts presence p to a binary state:

$$B_{i,t} = \mathbb{1}\left(p_{i,t} \geq \tau\right), \quad \tau = 0.16 \tag{1}$$

The threshold is not a free choice and should not be read as one. It was selected by sweeping τ from 0.02 to 0.98 and maximising F1 against City of Cape Town roof polygons acquired through January 2023, evaluated only within 2 km of a surveyed roof, because beyond that distance the absence of a roof polygon is missing data rather than evidence of no building. Over that 15,252,263-cell domain, containing 1,248,524 reference cells, the selected $\tau = 0.16$ scores F1 0.4441, precision 0.3119 and recall 0.7710.

Two consequences follow, and neither is cosmetic. The threshold is deliberately permissive: against the municipal layer it accepts roughly two false positives for every true one in exchange for retaining 77% of surveyed roof area, which suits a study of where building occurs rather than of how much of it there is. And the 2023 municipal layer that calibrates τ is not independent of the 2023 Open Buildings state that later supplies the hindcast target, so the presence threshold and the quantity it is scored against share evidence. Sensitivity of the headline results to alternative thresholds has not been tested; it is listed as a required experiment in Section 6.2.

A three-year temporal median suppresses isolated annual spikes. At the start and end of the sequence the nearest available annual state is repeated:

$$M_{i,t} = median(B_{i,t-1},\ B_{i,t},\ B_{i,t+1}) \tag{2}$$

The cleaned history retains a cell at year *t* only if its median-filtered state remains present through 2023:

$$C_{i,t} = min(M_{i,t},\ \ldots,\ M_{i,2023}). \tag{3}$$

This suffix-persistence rule guarantees a monotone built sequence and rejects temporary detections, but it is asymmetric: an early cell must survive more future checks. Cleaned states are therefore used to learn transition location and to hindcast morphology, whereas raw annual areas are used to estimate the recent areal growth rate. Figure 2 shows that the cleaning is not a purely cosmetic operation.

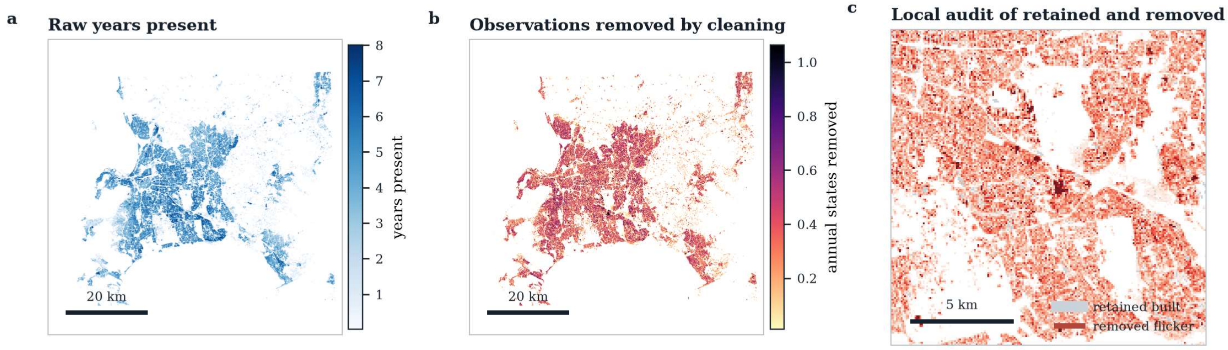

Figure 2. Temporal cleaning of the annual stack. (a) Number of raw annual states in which each cell is present. (b) Intensity of observations removed by the median and suffix-persistence rules. (c) Local audit of retained built fabric and removed flicker. The widespread low-intensity corrections explain why raw area and cleaned transition location serve different purposes.

The quantity that every later section is fitted to is the difference between the cleaned 2016 and 2023 states, and it is worth looking at before it is modelled. Between those two years the cleaned stack gains 1,005,175 cells, about 100.5 km². That area does not arrive as a small number of large new districts. It arrives as a fine accretion distributed around almost the whole built perimeter and through the interstitial gaps of the existing fabric, together with a smaller number of compact new blocks on the northern and eastern fringe (Figure 3). The grain of the change matters as much as its total, and Section 4.4 returns to it, because it turns out to determine what an edge-driven allocator can and cannot recover.

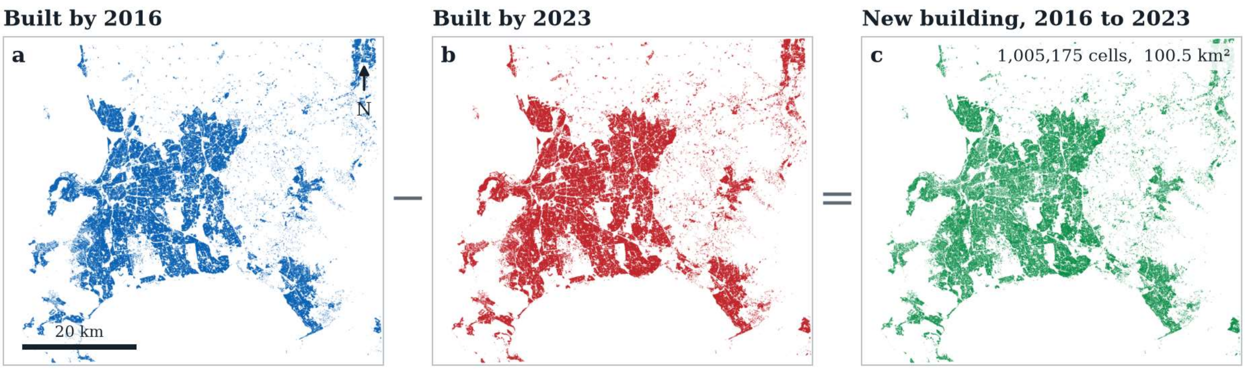

Figure 3. Observed change in the cleaned stack. (a) Cells built by 2016. (b) Cells built by 2023. (c) The difference between them, which is both the evidence from which the location model of Section 3.3 is fitted and the target of the hindcast of Section 3.8. Ink density is the share of each 40 m display block that is occupied. Panel (c) uses a more sensitive density scale than (a) and (b), because seven years of change is roughly two orders of magnitude sparser than the stock it is added to.

3.2 Developability and constraint separation

Terrain, flood, and water are kept outside the urban-pattern regression. For terrain-render luminance *L*,

$$u_i = clip((L_i - 25) / 230,\ 0,\ 1) \tag{4}$$

and the fitted terrain multiplier is

$$T_i = max(\exp(-5.00\ u_i^{0.88}),\ 0.004). \tag{5}$$

The response was fitted by weighted least squares to log relative build rates within distance-to-edge bands. Conditioning on distance matters because difficult terrain is systematically farther from existing development. Event counts provide approximate inverse-variance weights for the log rates. The flattest to brightest terrain band within 200 m of the edge changes from a 14.07% observed build rate to 0.21%, a roughly 67-fold suppression.

Flood-render intensity receives a mild piecewise-linear multiplier F: unmarked cells equal 1, values decline to 0.55 at intensity 120, and remain at 0.55 above that point. This is weaker than the observed relative suppression because the render partly captures water channels already excluded by the water mask. Let W equal 0 on water or outside the valid frame and 1 otherwise. Developability is

$$D_i = W_i \, T_i^{\gamma} \, F_i, \quad \gamma = 1. \tag{6}$$

Figure 4 reconstructs the aligned components on a white paper background. Figure 5 shows the evidence and sensitivity that justify their relative treatment.

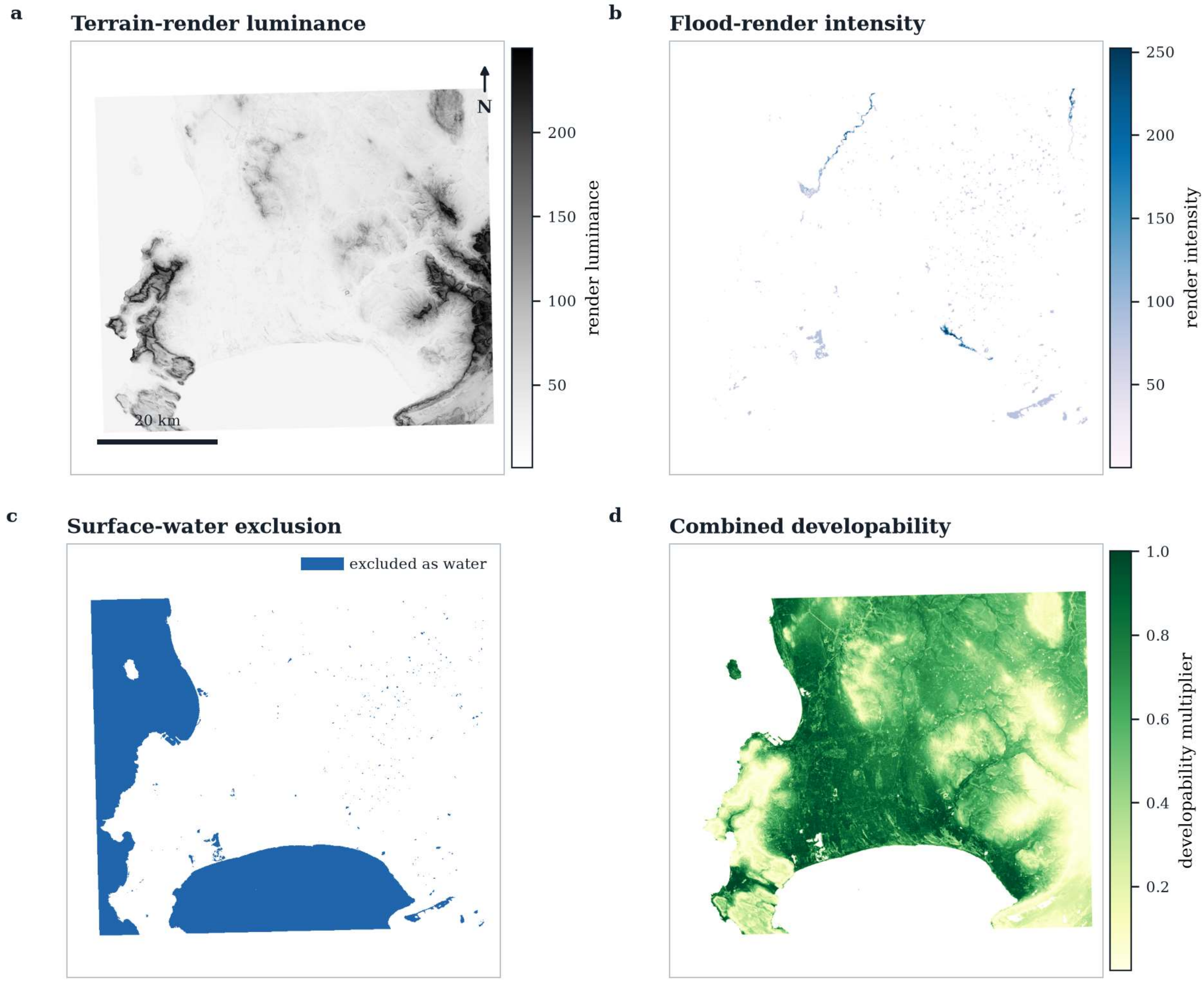

Figure 4. Environmental constraint stack. (a) Terrain-render luminance. (b) Flood-render intensity. (c) Surface-water exclusion at a render luminance of 60. (d) Combined developability D from Equation 6, a multiplier between 0.004 and 1. Off-domain and excluded cells are paper white; the panels show aligned model inputs rather than black presentation canvases.

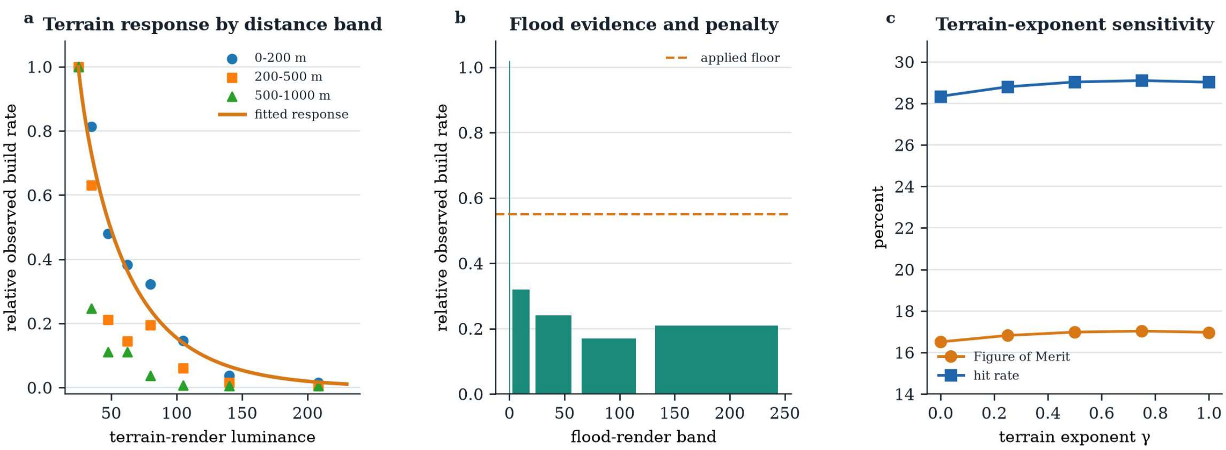

Figure 5. Empirical constraint evidence. (a) Terrain response measured within three distance-to-edge bands and fitted response. (b) Relative observed build rates in flood-render bands and the deliberately mild applied floor. (c) Hindcast sensitivity to terrain exponent γ. The selected γ = 1 has 16.97% Figure of Merit, only 0.06 percentage points below the sweep maximum at γ = 0.75.

3.3 Dynamic urban-pattern model

The location model is a binned-indicator logistic regression fitted on land with terrain luminance below 55. Four predictors are calculated from the current built state:

- distance to the nearest built cell;
- built fraction in an approximately 120 m local neighbourhood;
- built fraction in an approximately 600 m neighbourhood; and
- immediate adjacency to the built edge.

Each predictor enters as a set of binned indicators rather than as a continuous term, so the shape of each response is estimated from the data rather than assumed in advance. One shape constraint is nevertheless applied afterwards, and it is described below. Distance uses 12 bins to 3000 m and each density predictor uses 10 bins; adjacency is a single indicator. The fit is case-control: 880,780 observed 2016–2023 transitions on eligible land are contrasted with 2,119,220 sampled control cells drawn from the 13,954,372 eligible cells. For indicator vector **x** and coefficients β,

$$\eta_{i,t} = \beta_0 + \sum_{j=1}^{J} \beta_j \, x_{i,t,j}. \tag{7}$$

Because the fit is case-control, the intercept β_0 reflects the sampling ratio rather than any absolute transition rate, and it is discarded. What the simulation consumes is the exponentiated linear predictor, a **relative rate multiplier** rather than a probability, positive everywhere within the eligible candidate domain:

$$P_{i,t} = \exp\left(\sum_{j=1}^{J} \beta_j \, x_{i,t,j}\right). \tag{8}$$

P is therefore a ratio, not a chance: a cell with $P = 10$ is ten times as likely to be selected in a given step as an otherwise identical cell with $P = 1$, and *P* is not bounded above by one. On the observed 2023 state it ranges from 0 to 69.6. The zero is not a value of the exponential, which cannot reach it; it is the separate eligibility mask described two paragraphs below, applied on top of the multiplier. This distinction matters because *P* is used directly as a sampling weight in Equation 14, where the difference between a rate multiplier and a squashed probability changes the relative weights and not merely their scale.

Binned indicators estimate shape, but they also allow a bin holding a handful of observations to receive a coefficient that is noise, and on these data the raw fit did exactly that at the far end of the distance range. The observed build rate is 0.043% in the 750–1200 m band and exactly zero beyond 1200 m, yet the fitted relative rate multiplier rose across the last three bands instead of falling. A model carrying that tail would seed new settlements three kilometres from anything.

The production scorer therefore applies a count-weighted isotonic projection to two of the four coefficient curves, after the logistic fit and before any simulation. For a fitted curve β over bins $j = 1 \ldots J$ with bin counts *n*, the projected curve *b* that replaces it is

$$b = \mathrm{argmin}_m \sum_{j=1}^{J} (n_j + 1) \, d_j^{\,2}, \qquad d_j = m_j - \beta_j, \qquad m \in M \tag{9}$$

where *M* is the set of curves that are non-increasing over the distance bands, and separately the set that is non-decreasing over the neighbourhood-density bands; this is the standard weighted isotonic regression [15]. Well-populated bins are essentially unchanged; sparse bins are pulled into line with their neighbours rather than inventing structure. Adjacency is a single indicator and needs no ordering. The local built-share curve is deliberately left unconstrained, because once distance and adjacency are accounted for the measurement says it is close to flat, and imposing a direction on it would assert something the data does not support. Figure 6 shows the evidence and the size of the correction.

This is a genuine shape constraint applied after fitting, not numerical cleanup, and it can change the ranking of candidate cells. Three limits on what is reported here must be stated with it. The production coefficients were not archived separately from the fitted model object, so Figure 6 is computed from the spatially blocked diagnostic refit of Section 3.4 over the same predictors, the same bins and the same evidence; it reproduces the mechanism and its magnitude rather than production's exact coefficients, and the two fits are close but not identical, with diagnostic and production adjacency coefficients of 2.0608 and 2.0868. The assumed directions are defensible rather than proven: build rate is not expected to rise with distance from existing building, nor to fall as surrounding density rises, and the observed rates in Figure 6 are consistent with both, but consistency is not a test. And the hindcast has not been repeated with the projection disabled, so this paper cannot say how much of the result in Section 4.2 depends on it. That experiment is named in Section 6.2.

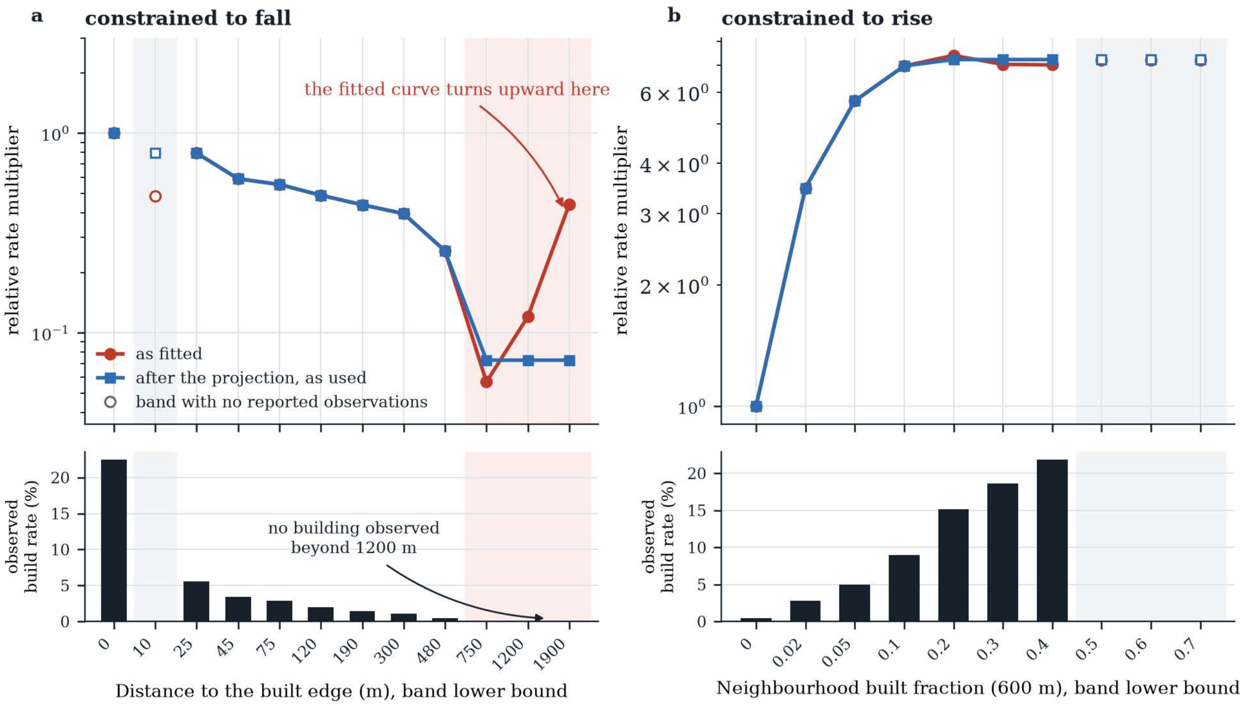

Figure 6. Why two of the four coefficient curves are constrained after fitting. Upper panels: the fitted relative rate multiplier for each band, as the regression produced it (red) and after the projection of Equation 9 (blue). Lower panels: the share of cells in each band that were actually built on between 2016 and 2023. The two rows are read together. In (a) the observed build rate falls to 0.04% in the 750–1200 m band and to exactly zero beyond 1200 m, yet the fitted curve turns upward across those last three bands, shaded pink, and ends higher than it was at 480 m. The upturn is an artefact of fitting, not a signal: those three bands contain about 470 observed transitions between them and none at all beyond 1200 m, so the regression has almost nothing to pin them down, and a model that kept the upturn would seed new settlement three kilometres from anything. The projection replaces it with the flat blue line. In (b) the fitted curve is already close to monotone and the projection barely moves it, which is the expected outcome when a curve is well supported. Grey bands are bins absent from the archived per-bin summary; they carry no weight in the projection and their markers are hollow. Curves are from the diagnostic refit of Section 3.4 rather than the production fit, over the same predictors, bins and evidence, so they reproduce the mechanism and its size and not production's exact coefficients.

Two implementation limits belong with the definition. First, the two neighbourhood predictors are evaluated on a 40 m grid and bilinearly upsampled before allocation at 10 m; the fields are smooth at hundreds of metres, so the approximation is small, but it means the neighbourhood terms are not resolved at the full analysis scale. Second, the score is set to exactly zero beyond 3000 m from the nearest built cell. This bounds the candidate set and makes a century of annual steps affordable, but it is also a hard structural limit: no cell further than 3 km from existing building can ever be selected, by any mechanism in the model, including the detached-growth pool of Section 3.5.

Terrain and flood do not appear in Equation 7. This makes the constraint response auditable and allows γ to be varied without refitting the urban-pattern model. The predictors in Figure 7 operate at different spatial scales and are recalculated after every allocation.

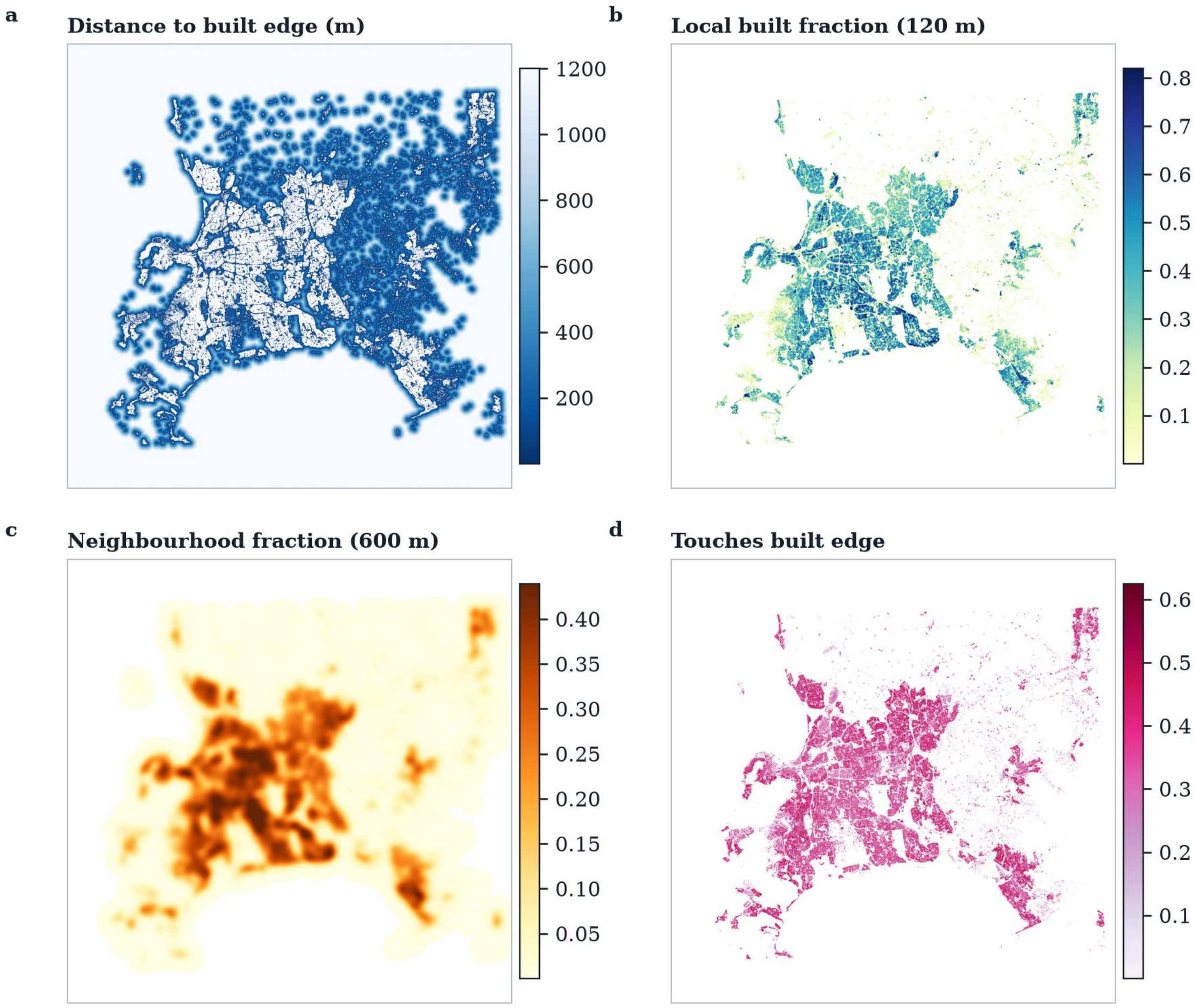

Figure 7. Dynamic predictors from the 2016 built state. (a) Distance to the built edge. (b) Local built fraction within approximately 120 m. (c) Neighbourhood built fraction within approximately 600 m. (d) Immediate adjacency to the built edge. Cells that were already built in 2016 are paper white in every panel, because the predictors are defined only for candidate cells. Each simulated step changes these surfaces before the next allocation.

3.4 Spatially blocked classifier diagnostic

The production rank model does not require a calibrated intercept, classification threshold, or confusion matrix. A separate diagnostic therefore refits the same four predictor families with an intercept, in probability form, and evaluates whole 640 m blocks held out from training. Thirty-five percent of blocks are assigned to the test partition; up to 3 million cells per side are sampled. The F1 threshold is selected on the held-out probability curve for descriptive purposes only. This diagnostic measures the ranking information in the predictors. It does not simulate annual feedback, demand, constraints, direction, or stochastic allocation, and its probability scale is not the scale on which the simulation allocates.

Three further limits belong here rather than in a footnote, because they bear directly on how Section 4.1 should be read. First, the diagnostic does not apply the monotone projection of Equation 9, so it evaluates the predictor family and the binned fit rather than the scorer the allocator actually consumes. Second, blocks are assigned to train and test by a single random permutation with no buffer between them; because one predictor summarises built fraction over roughly 600 m, a test block lying directly against a training block can share information with it across their common boundary, and a single split gives no estimate of how much the result would move under a different one. Third, the maximum-F1 operating threshold is selected on the held-out precision–recall curve and then reported on those same held-out cells, so F1, precision and recall are optimistic by an amount this design cannot measure. ROC-AUC and PR-AUC are threshold-free and are unaffected by that last point. The correct design is a buffered, repeated spatial cross-validation with the threshold chosen inside the training partition and applied once to untouched test cells. It has not been run.

3.5 Suitability, directional tilt, and detached growth

Base suitability is the transparent product of pattern pressure and developability:

$$S_{i,t} = P_{i,t}\ D_i. \tag{10}$$

Figure 8 shows that both a plausible urban relationship and usable land are required.

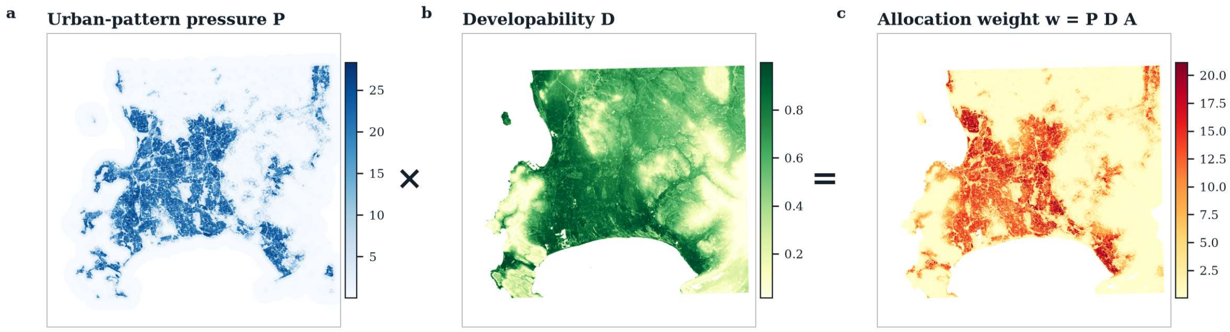

Figure 8. Construction of the allocation weight. (a) Dynamic urban-pattern pressure P. (b) Fixed developability D. (c) The allocation weight w = P D A, including the directional multiplier of Equation 11. The urban-pattern surface is recomputed as the simulated city changes; developability remains fixed. Note that P and w are relative rate multipliers and are not bounded by one.

A weak directional multiplier is measured from the 2016–2023 displacement of new building. For bearing θ from the built centre,

$$A_i = 1 + 0.20 \cos(\theta_i - 45.4°). \tag{11}$$

The amplitude of 0.20 was selected by retrospective vector-error testing over the amplitudes 0, 0.2, 0.4, 0.6 and 0.8: it minimises the error between the simulated and observed displacement of the growth centroid, at 1.29 km against 4.26 km for an isotropic model. It is not a claim that every local transition proceeds north-east, and it is not free: the isotropic model scores a marginally higher Figure of Merit (16.99% against 16.97%), so the directional term improves growth direction at a very slight cost in cell-level agreement. The residual directional error that remains after this calibration is reported in Section 4.2.

The origin of θ has to be stated precisely, because the directional numbers are sensitive to it and the code is not consistent about it. The archived calibration measures the displacement of the centroid of new building from a centroid of the 2016 built *mass*, at easting 280097.1 and northing 6238927.9 in EPSG:32734, which is what yields the 45.4° bearing and the 2.21 km offset. The centroid of the cleaned *binary* 2016 mask lies about 1.3 km away, at easting 279715.3 and northing 6240163.4, and the same displacement measured from there is 80.8°. The simulation recentres its directional field on the current binary built state at every step, so the origin that allocates is a moving version of the second, not the first. Every figure and number in this paper uses the archived mass-weighted origin, because that is the one the published run was calibrated against, but the three definitions have not been reconciled and the calibration has not been repeated under a single one. This is recorded as an unresolved item in Section 6.2.

Detached growth is handled by a separate pool that receives 2.8% of each step's demand and places it beyond 300 m from the built edge. The pool is not scattered cell by cell: the budget is divided between ten new nuclei per step, each grown as a compact settlement, so that detached development arrives as patches rather than as isolated pixels. Without this mechanism the fitted model produces almost no detached growth at all, because the adjacency term dominates every comparison. Two caveats follow. The 2.8% share reproduces the observed 2016–2023 detached share by construction and therefore cannot be treated as independent validation. And the pool remains subject to the 3 km candidate limit of Section 3.3, so it relocates growth within the metropolitan fringe rather than founding genuinely remote settlements.

3.6 Independent demand and saturation damping

The spatial model answers *where*; the demand module answers *how much*. The three rules are given in Table 2.

Table 2. Demand scenarios. Each rule is supplied independently of the location model, so the same suitability surface allocates all three. The low rule uses a different product from the central rule and therefore a different definition of built area.

Scenario	Nominal rule	Source and interpretation
Low	3.44 km² yr⁻¹	long-run GHSL areal increment
Central	5.71 km² yr⁻¹	raw Open Buildings increment, 2016–2023
High	1.79% yr⁻¹ compound	continuation of the recent proportional rate

Let R_t be remaining developable area, R_0 its starting value of 1084.9 km², and q_t nominal demand. The land-availability damping is

$$f_t = R_t / R_0, \quad q*_t = min(q_t\ f_t,\ R_t). \tag{12}$$

For the high scenario the nominal demand over a Δ-year step is proportional to the built area U_t at the start of the step:

$$q_t = U_t[\exp(\Delta \ \ln(1 + 0.0179)) - 1]. \tag{13}$$

The model advances annually through 2036 and in five-year steps thereafter. Damping prevents an impossible allocation after suitable land is consumed, but it is not a demographic or economic law.

3.7 Stochastic allocation and state update

For eligible normal-pool cells, the weight is

$$w_{i,t} = S_{i,t}\ A_i. \tag{14}$$

Each step selects k_t cells by the Gumbel top-*k* method for weighted sampling without replacement [17]. With independent V_i ~ Uniform(0,1) and a selection temperature λ,

$$g_i = -\log(-\log V_i), \quad z_{i,t} = \log w_{i,t} + \lambda g_i, \quad \lambda = 0.35. \tag{15}$$

The k_t largest z values are selected. At $\lambda = 1$ this is exactly the Gumbel top-k identity and selection is proportional to w. The production runs use $\lambda = 0.35$. Because dividing every score by λ leaves the ordering unchanged, this is equivalent to proportional sampling on $w^{1/\lambda}$, that is on approximately $w^{2.86}$. The consequence is a sharper selection front than proportional sampling would give: high-weight cells are taken more reliably, replicates agree with one another more than they otherwise would, and the model is correspondingly less willing to place growth on moderately weighted land. This parameter is therefore not a cosmetic noise setting, and every result reported below is conditional on it. Its effects are revisited in Sections 4.3, 4.4, 4.6 and 6.2. The detached-growth nuclei of Section 3.5 are drawn at $\lambda = 1$.

Built state, distance, adjacency, neighbourhood density, remaining land, and suitability are then updated before the next step. R = 12 replicates use the same fitted model and demand rule but different random seeds derived from a fixed master seed of 20260802. If $Y_{i,h,r}$ is 1 when replicate r has selected cell i by horizon h,

$$Pr_{i,h} = (1/R) \sum_{r=1}^{R} Y_{i,h,r}, \quad R = 12. \tag{16}$$

Replicate agreement is reported in Section 4.6 and needs an explicit definition, because more than one is defensible and the choice changes the number by a factor of three. Let $N_{h,r}$ be the set of cells that replicate r has selected as new by horizon h. The reported statistic is

$$A_h = |N_{h,1} \cap \dots \cap N_{h,R}| \; / \; |N_{h,1} \cup \dots \cup N_{h,R}| \tag{17}$$

that is, the share of every cell any replicate selects that all replicates select. It is an all-run intersection over union. It falls mechanically as replicates are added, so it is not comparable across ensembles of different size, and with R = 12 a per-cell probability can only take the thirteen values 0, 1/12, …, 1. Whether the probability surfaces and the statistics derived from them have converged at twelve replicates has not been tested. Section 4.6 also reports the intersection as a share of one run's new area, which is the more intuitive reading of the same three quantities.

Probability, an area-matched consensus, and one representative realization are stored separately. The representative map is a coherent simulated future; the probability surface describes conditional spatial pressure; the consensus is a ranked summary and can overemphasise areas where replicates agree.

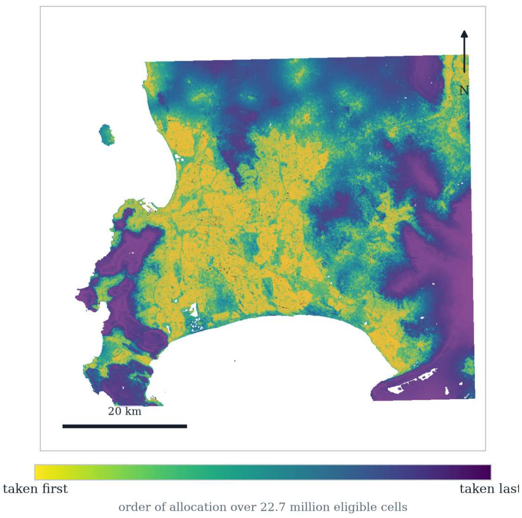

Figure 9. Order of allocation under repeated re-scoring, with the demand rule removed. Gold is taken first and purple last. The map carries no dates and is not a forecast; it is a diagnostic of the fitted model's preference ordering over the whole eligible landscape.

A property of the iteration is easier to see than to state. If the demand rule of Section 3.6 is set aside and the allocator is run until no eligible cell is left, the order in which land is taken becomes a complete summary of what the fitted model believes about the landscape. That saturation run consumes 22.7 million eligible cells, of which 150 are placed by the fallback rule rather than by the model.

Two behaviours that no single-horizon map shows are explicit in Figure 9. The first is that allocation propagates outward from existing fabric in rings, so the order is governed largely by distance to the 2016 edge rather than by absolute suitability: land of high intrinsic developability that happens to be remote is taken late. The second is that the terrain and flood factors of Equation 6 do not forbid the mountain slopes, the Peninsula spine or the eastern ranges. They place them last. Both behaviours are consequences of the model's structure rather than of its calibration, and both reappear as errors in Sections 4.2 to 4.4.

3.8 Retrospective validation design

The end-to-end hindcast begins from the cleaned 2016 state. At each annual step it receives the actual cleaned quantity of new cells and runs the complete iterative allocator. The target contains 1,005,175 new cells by 2023, about 100.5 km², or roughly 14.4 km² per year. That rate is about 2.5 times the 5.71 km² yr⁻¹ central forecast demand, because the two are measured on different stacks: the hindcast target counts cells that persist under the cleaning of Section 3.1, whereas the demand rules of Section 3.6 use raw annual built area. The two numbers are not in conflict, but they are not interchangeable either, and the difference is taken up again in Section 6.2.

A hit H is predicted and observed change, a miss M is observed change not selected, and a false alarm F is selected change not observed. Figure of Merit is [12]

$$FoM = H/(H + M + F). \tag{18}$$

Because predicted and observed quantities are equal, precision, recall, and F1 are numerically equal to the hit rate, and M and F are necessarily equal to one another. This is an in-period reconstruction: the location model and directional calibration use 2016–2023 evidence. It is not a temporally independent forecast test. A uniform random baseline and a no-terrain version use the same demand.

Cell-level agreement is not the only thing worth scoring. The hindcast also records the displacement of the centroid of new growth from the centroid of the 2016 built state, which tests whether the simulated city grows in the observed direction, and the split of new cells between infill, edge expansion, fringe and leapfrog, which tests morphology. All three are reported in Section 4, including where they disagree with the observations.

3.9 Error-structure diagnostics

Section 4.4 reports two descriptive diagnostics of the hindcast errors, and both are computed from the reconstructed replay masks rather than from any separate model fit.

Detachment is the Chebyshev, or chessboard, distance in cells from the cleaned 2016 built mask, converted to metres at 10 m per cell, so that a cell touching the 2016 edge orthogonally or diagonally is at 10 m. Observed new cells are grouped into bands with lower bounds at 10, 20, 40, 80, 160, 320 and 640 m, the last band being open-ended.

Patch size is the area of the connected component of *observed* change that each observed new cell belongs to, under 8-connectivity, in hectares. Bands are under 0.1, 0.1 to 0.5, 0.5 to 2, 2 to 10, 10 to 50, and over 50 hectares.

In both cases the reported quantity is a cell-weighted recall: within a band, the number of observed new cells the simulation also selected, divided by the number of observed new cells in that band. It is not the share of patches detected, and a large patch of which the model selected a thin edge still contributes its whole area to the denominator. The two variables are strongly correlated, since cells in large patches are on average further from the 2016 edge, so the two curves are two views of one failure and not two independent mechanisms. Both are descriptive summaries of the same in-period reconstruction that produced the Figure of Merit, computed after the fact, with no held-out data and no significance testing.

The four windows in Figure 15 are selected by the same masks. Missed-cell density is summed over 4 km square windows on a 320 m coarsened grid; a window is eligible only if at least 8% of it was already built in 2016, which keeps the panels on the urban fringe rather than on open ground or open water; the four highest-scoring eligible windows are taken in turn with a 12 km minimum separation. They are therefore selected on the error outcome itself and are illustrations of a pattern quantified elsewhere, not a sample from which anything should be estimated.

4. Urban forecast results

4.1 Classifier information in spatial holdout

The blocked diagnostic uses 3 million training cells and 3 million test cells with a held-out base rate of 0.063. The design limits of Section 3.4 apply to every number in this subsection: it is one unbuffered split of a refit that omits the monotone projection, and its threshold-dependent metrics are selected and reported on the same held-out cells. ROC-AUC is 0.880 and PR-AUC 0.307; these are threshold-free. Best F1 is 0.456, precision 0.343, recall 0.680, Brier score 0.0477, and precision lift 5.40 relative to the base rate; these four should be read as an upper estimate, because the threshold that produces them was chosen on the same cells. Figure 10 reports these values as a predictor diagnostic. They are not the hindcast score.

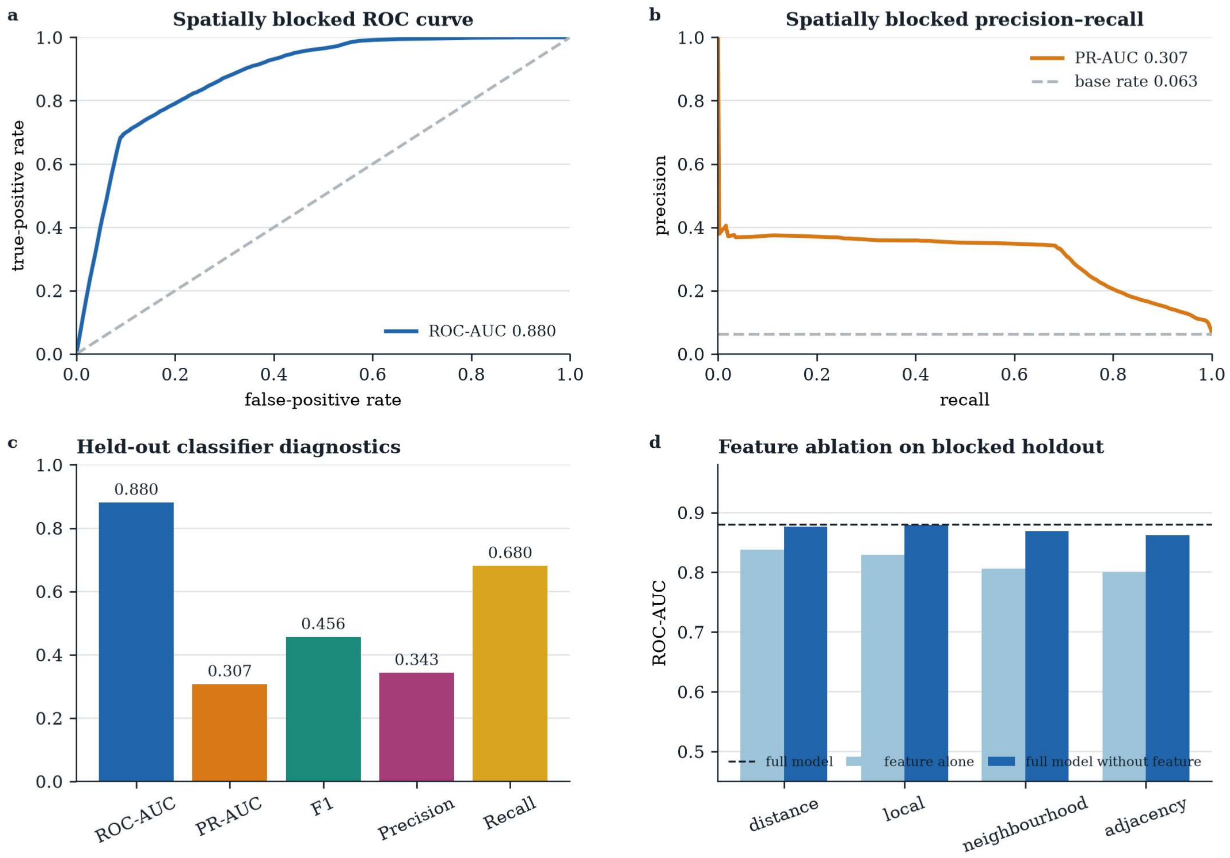

Figure 10. Spatially blocked classifier diagnostic. (a) ROC curve. (b) Precision–recall curve against the 0.063 base rate. (c) Held-out summary metrics at the maximum-F1 threshold. (d) Single-feature and leave-one-feature-out ROC-AUC. Whole 640 m blocks, rather than randomly mixed neighbouring cells, define the holdout, but they are not buffered and the split is not repeated [14].

4.2 End-to-end hindcast

The archived production run records 291,686 hits, 713,489 misses, and 713,489 false alarms. The hit rate is 29.02% and FoM is 16.97%. Removing the terrain constraint reduces FoM to 16.52%; uniform random allocation produces 2.16%. The full-model FoM is therefore 7.9 times the uniform-random value.

The production run did not retain its exact simulated mask. A later replay using the archived fitted weights and seed produced a mask for visualisation, with 292,324 hits and 17.02% FoM. The small stochastic replay difference is disclosed; the official bars and manuscript headline retain the archived production values. See Figure 11.

The same run also scores the direction of growth, measured from the archived mass-weighted 2016 origin of Section 3.5, and here the model does noticeably less well. Between 2016 and 2023 the centroid of observed new building sat 2.21 km from the centroid of the 2016 built state, on a bearing of 45.4°. The simulated growth centroid sat 1.60 km away on a bearing of 10.5°. The model therefore reproduces roughly three-quarters of the observed displacement but misses its bearing by about 35°, growing too evenly around the existing city and too little towards the north-east. The directional multiplier of Equation 11 reduces this error substantially, from 4.26 km of vector error for an isotropic model to 1.29 km, but it does not remove it. This is the clearest evidence that the four urban-pattern predictors contain no directional information: distance and density are isotropic by construction, so any consistent directional signal has to be supplied from outside them, and a single global bearing is a crude way to supply it.

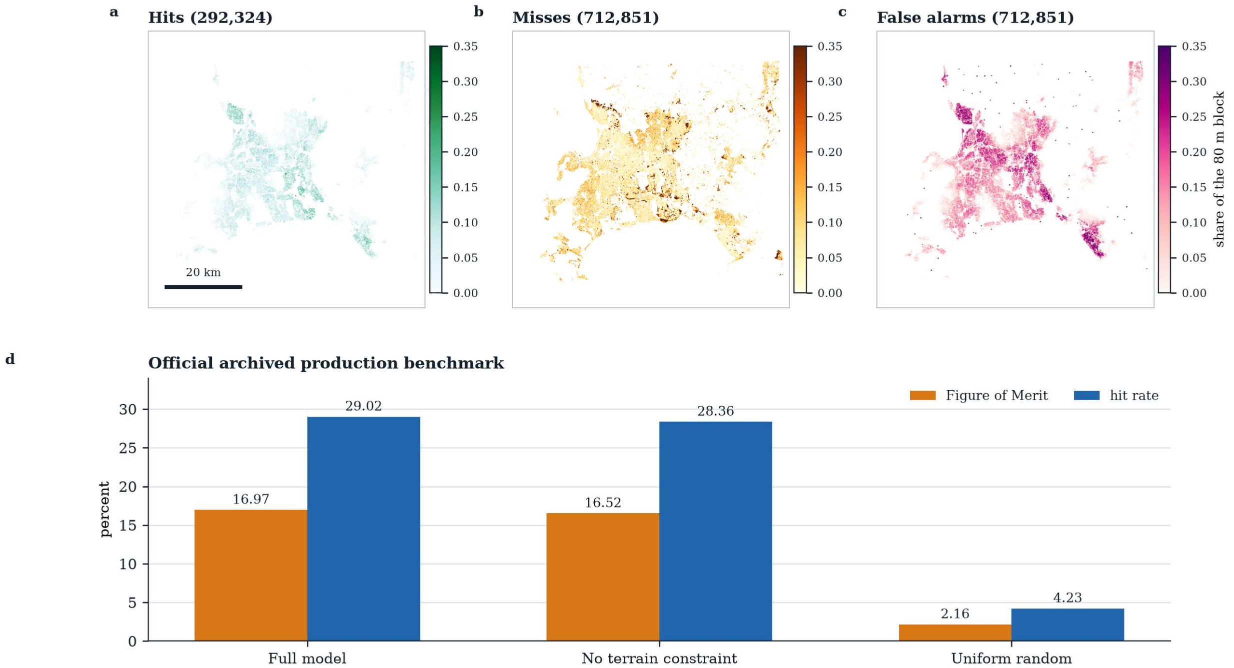

Figure 11. End-to-end hindcast. (a) Hit density, (b) miss density, and (c) false-alarm density in the reconstructed 2016–2023 replay, each as the share of the 80 m display block on a common scale. The three categories are interleaved at 10 m, so they are shown separately rather than as one three-colour map, in which every block would be a mixture. Misses concentrate on the northern and north-eastern fringe and false alarms in the established central fabric, which is the spatial signature of the infill overprediction of Section 4.3 and the directional shortfall of Section 4.2. (d) Official archived production benchmarks. Counts in (a)–(c) are from the replay, which obtained 17.02% FoM; the bars and the reported headline retain the archived production 16.97% FoM.

Figure 12 redraws the same three classes at the analysis resolution and side by side rather than as densities over a display block, and the three then have visibly different geometry. Hits form a thin connected tracery that follows the 2016 perimeter and threads through the interstitial gaps of the established fabric. Misses form solid districts, concentrated on the northern and north-eastern fringe and in the dense south-eastern settlement belt, and they are the only one of the three classes that is coherent at the scale of a suburb. False alarms form a halo around and inside the existing built area, which is the same overprediction of infill that Section 4.3 measures as a mode share.

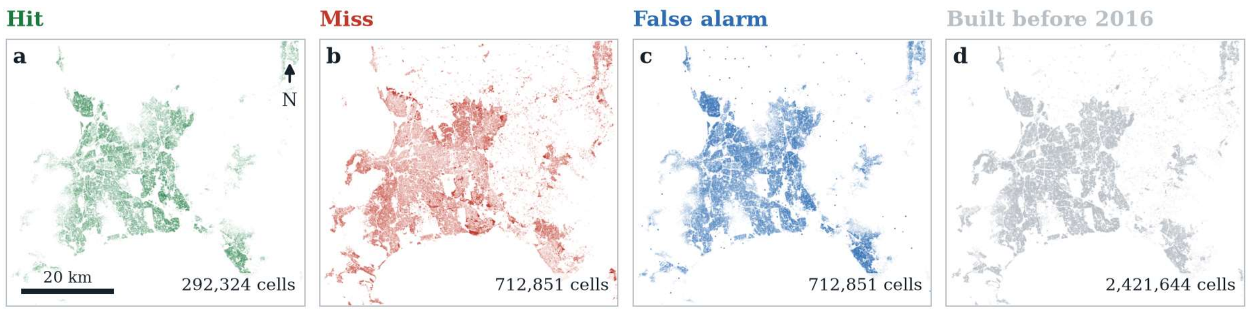

Figure 12. The scored classes drawn apart. (a) Hits. (b) Misses. (c) False alarms. (d) The pre-2016 stock, shown for orientation and never scored. All four are at the analysis grid, aggregated to 30 m display blocks with ink density proportional to block coverage. Misses and false alarms are equal in number by construction, because the hindcast is supplied with the observed quantity at every step, so the difference between (b) and (c) is entirely one of location. Counts are from the reconstructed replay described in Section 4.2 and sum to its 17.02% Figure of Merit, not to the archived production 16.97%.

The directional shortfall described above can be read the same way. Figure 13 separates two statistics that are easily confused. The marginal distribution of headings of individual new cells about the centroid of the 2016 built mass is strongly bimodal, along the north-west to south-east axis of the Cape Flats, and the simulation reproduces that bimodality closely; a model driven by distance and density will follow the shape of the city whether or not it has any directional information at all. The resultant of that distribution is a different quantity, and it is the one Equation 11 is calibrated on and the one the model gets wrong.

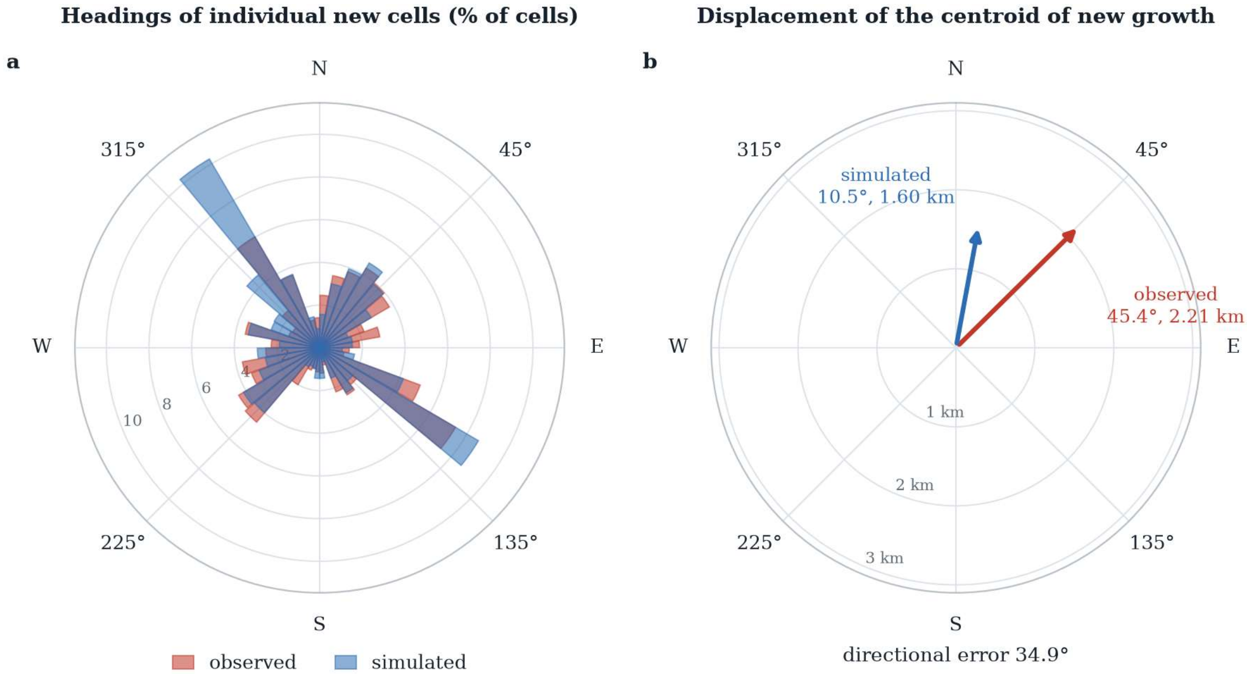

Figure 13. Direction of growth, observed against simulated. (a) Marginal distribution of the headings of individual new cells about the archived centroid of the 2016 built mass, in 10° bins, as a share of all new cells. The two lobes follow the north-west to south-east axis of the Cape Flats and are reproduced almost exactly by the simulation. (b) Displacement of the centroid of new growth from the same origin, which is the statistic Equation 11 is fitted to. Both panels are computed on the same 2016-2023 Open Buildings change that Equation 11 is calibrated on, so the distribution and the fitted bearing describe one body of evidence rather than two. The simulated displacement is both shorter and rotated approximately 35° anticlockwise of the observed one. Values in (b) are the archived production figures; the histograms in (a) are computed from the cleaned stack and the reconstructed replay mask.

4.3 Expansion morphology

Observed change is 17.55% infill, 72.66% edge expansion, 7.03% fringe, and 2.75% leapfrog. The simulation produces 29.59% infill, 67.48% edge expansion, 0.12% fringe, and 2.81% leapfrog (Figure 14). The allocator captures the dominant edge mode but is too willing to fill existing blocks and too reluctant to form low-density fringe patches. The leapfrog match is expected because that pool was assigned a fixed share.

Two model choices point in the same direction as this error. The selection temperature $\lambda = 0.35$ of Equation 15 concentrates selection on the highest-weight cells, and the highest-weight cells are by construction those with the greatest adjacency and neighbourhood density, that is interior gaps. The 3 km candidate limit of Section 3.3 then removes the far end of the distance range where fringe patches would otherwise form. Neither is a complete explanation, because fringe growth is a patch phenomenon and the main pool selects cell by cell, but both push allocation inward, and a fringe share of 0.12% against an observed 7.03% is the largest single structural failure in this paper.

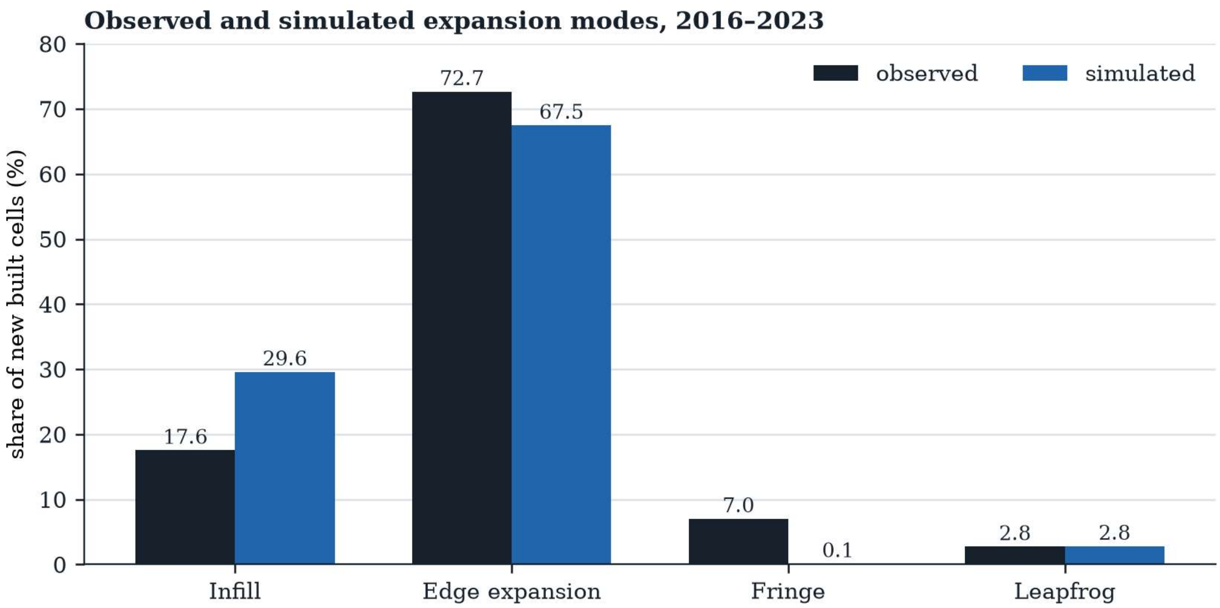

Figure 14. Observed and simulated 2016–2023 expansion modes. The model approximates edge expansion and the specified leapfrog share, overpredicts infill, and almost eliminates observed fringe growth.

4.4 Spatial structure of the hindcast errors

Mode shares describe the simulation. They do not say which parts of the observed record it failed to reach. Four 4 km windows, chosen automatically by the rule in Section 3.9 as the densest concentrations of missed cells that also contain established urban fabric, are shown in Figure 15. The pattern is consistent across all four and is not visible at metropolitan scale. Within established suburbs the model paints street frontage: fine blue and green filaments trace the road network, which is where the adjacency and local-density terms score highest. The large red blocks lie outside that fabric and are internally coherent, in several cases with a street layout of their own that has no counterpart in the surrounding blocks.

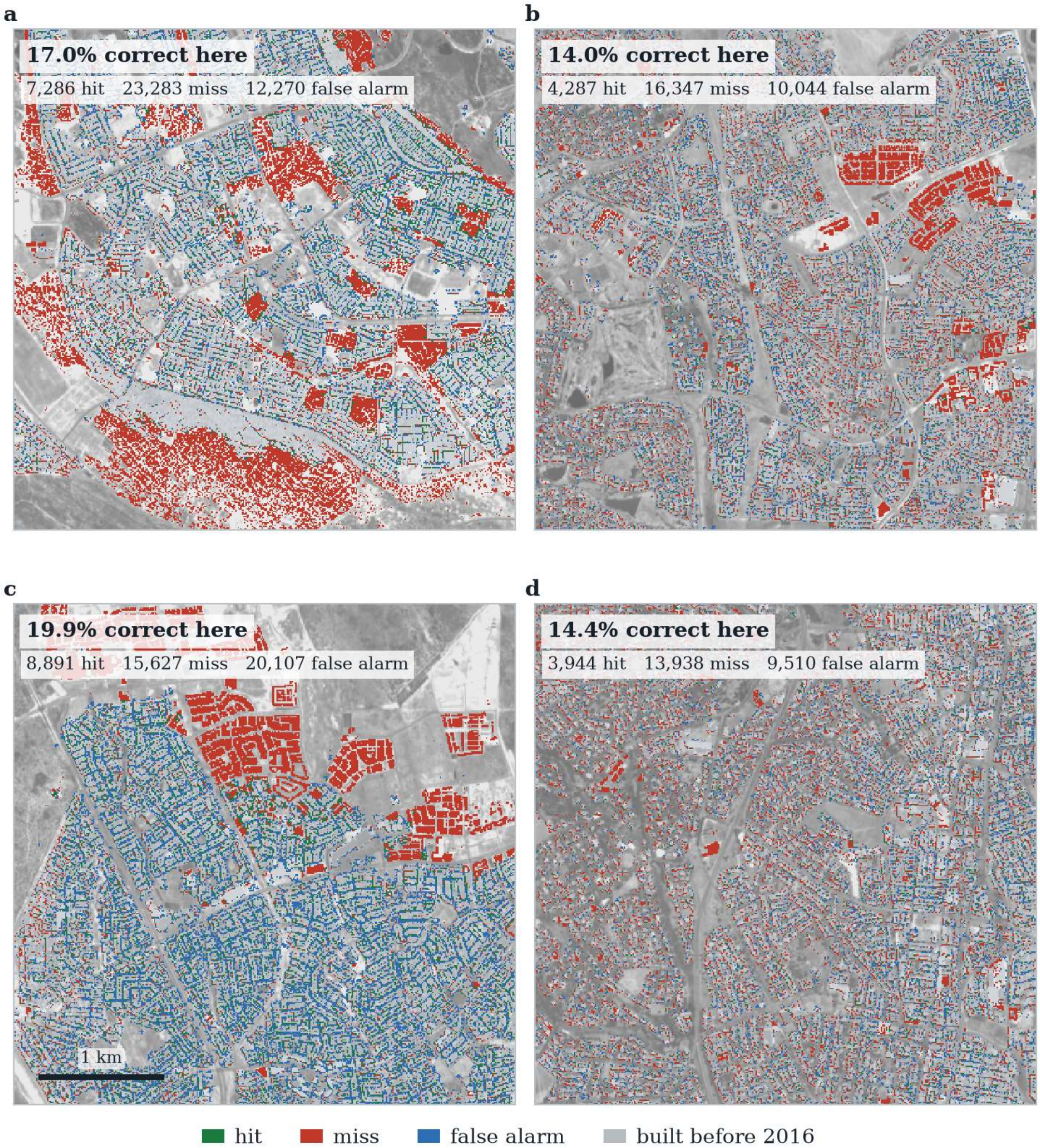

Figure 15. Four 4 km windows over the busiest concentrations of missed cells, at the 10 m analysis grid, on desaturated December 2023 imagery. Windows were selected automatically by the outcome-based rule of Section 3.9: missed-cell density summed over 4 km windows on a 320 m coarsened grid, restricted to windows at least 8% built in 2016, taken in turn with 12 km minimum separation. Percentages are the Figure of Merit within each window. Inside the established fabric the simulation follows street frontage; the missed areas are compact blocks outside it.

That observation was first made from the imagery rather than from the masks, and it has an obvious failure mode as an argument: any sufficiently determined reader of satellite pictures can find a story in them. Two things are therefore reported here. Figure 16(a)–(d) is visual interpretation of high-resolution imagery, four close views of missed districts. Their morphologies are not all of one kind. Panel (a) is a planned estate with a repeated unit and a single internal street loop, of the sort that appears complete within one annual observation. Panels (b) and (c) are unstructured settlement, dense and sparse respectively, with no street grid and no consistent building orientation. Panel (d) is a development front detached from the 2016 edge across open ground. What they share is not a building type. It is that none of them is an accretion onto an existing built edge.

Figure 16(e) and (f) test that directly from the archived masks, and the result is stronger than the visual argument. Recall against distance from the 2016 built edge collapses from 39.2% for cells in the first 10 m ring to 4.9% in the second, 0.2% in the third, and effectively nothing beyond, with a small recovery to 1.4% in the 320 m band produced by the detached pool of Section 3.5. Recall against the size of the connected patch of observed change that each cell belongs to falls monotonically from 36.6% for patches under 0.1 ha to 25.8%, 7.6%, 5.8%, 3.0% and finally 0.9% for patches larger than 50 ha. The 1,005,175 observed new cells form 295,536 connected patches under 8-connectivity. Both quantities are cell-weighted recalls, not patch detection rates, and the two are correlated, because cells in large patches sit further from the 2016 edge on average; they are two views of one failure rather than two independent mechanisms.

Neither relationship is a surprise given the structure of Section 3.3, and neither is by itself a fault: an edge-driven allocator that is handed the correct annual quantity will spend it at the edge. The point is what the two curves imply for interpretation. The 29.02% hit rate is not a uniform 29% chance of being right about any given piece of new building. It is close to 40% for the incremental thickening of an existing perimeter and close to zero for a new district, whatever that district's morphology. Every map in Section 4.6 onward inherits that asymmetry, and among the caveats in this paper it is the one that bears most directly on how the future maps should be read: as pressure surfaces rather than as site predictions. Both curves are descriptive and in-sample, in the sense of Section 3.9, and neither has been tested against an independent period.

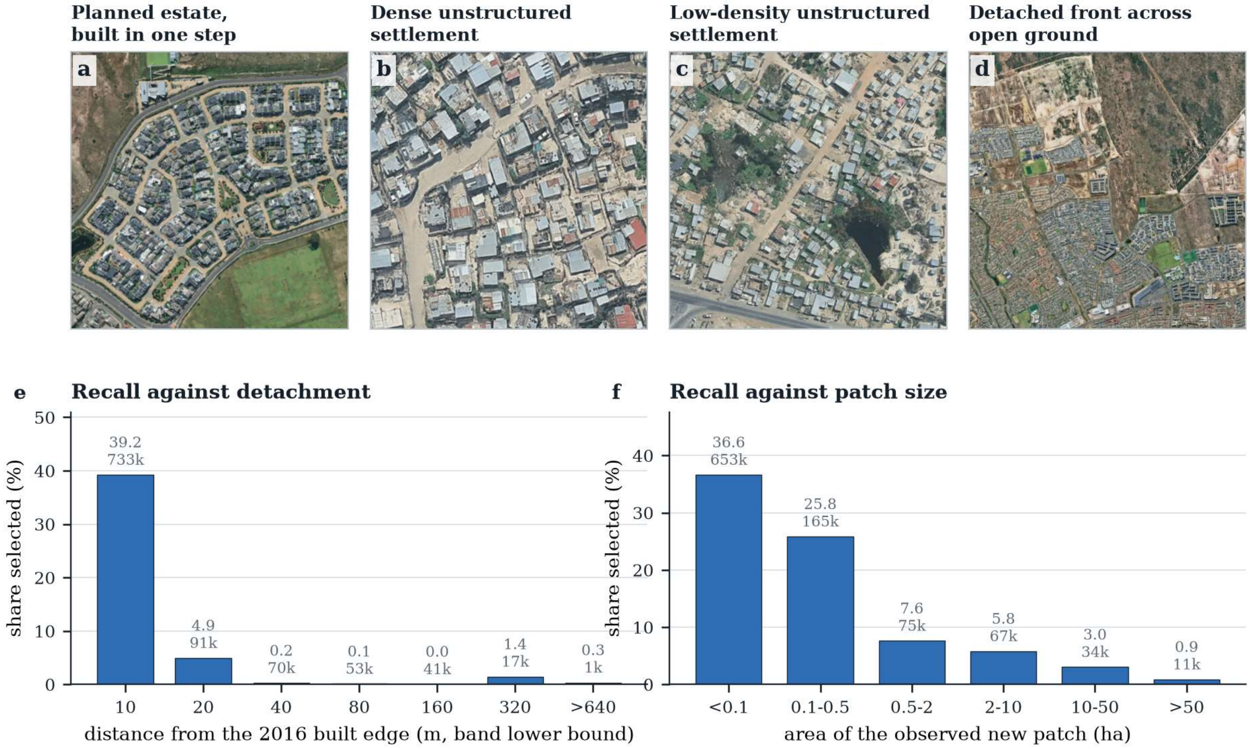

Figure 16. Morphology of the misses. (a)–(d) Four close views of districts the hindcast did not select, identified by visual comparison of missed clusters against high-resolution imagery: (a) a planned estate completed within one annual step, (b) dense unstructured settlement, (c) low-density unstructured settlement, (d) a detached development front. Imagery © Google; includes imagery from Google's third-party providers. The panels are outcome-selected illustrations, not a random or exhaustive sample, and the archived layers carry no capture date, coordinates or scale, so none is shown. (e) Share of observed new cells selected by the model, by Chebyshev distance from the 2016 built edge. (f) The same share by the area of the connected patch of observed change to which each cell belongs. Bar annotations give the percentage and the number of observed cells in the band. Panels (e) and (f) are computed from the archived masks and are reproducible from the code package.

4.5 Modelled 2026 baseline and scenario totals

The observation record ends in 2023 at 342.68 km² raw built area. Three central-scenario steps create a modelled 2026 baseline of 359.73 km². The baseline is not an observation. Under the central scenario, total built area is 414.7 km² in 2036, 609.4 km² in 2076, and 801.1 km² in 2126. New area after 2026 is therefore 54.9, 249.7, and 441.3 km². Corresponding low totals are 386.6, 511.7, and 647.1 km²; high totals are 428.0, 755.0, and 1136.0 km². Figure 17 reads these values directly from the archived run tables.

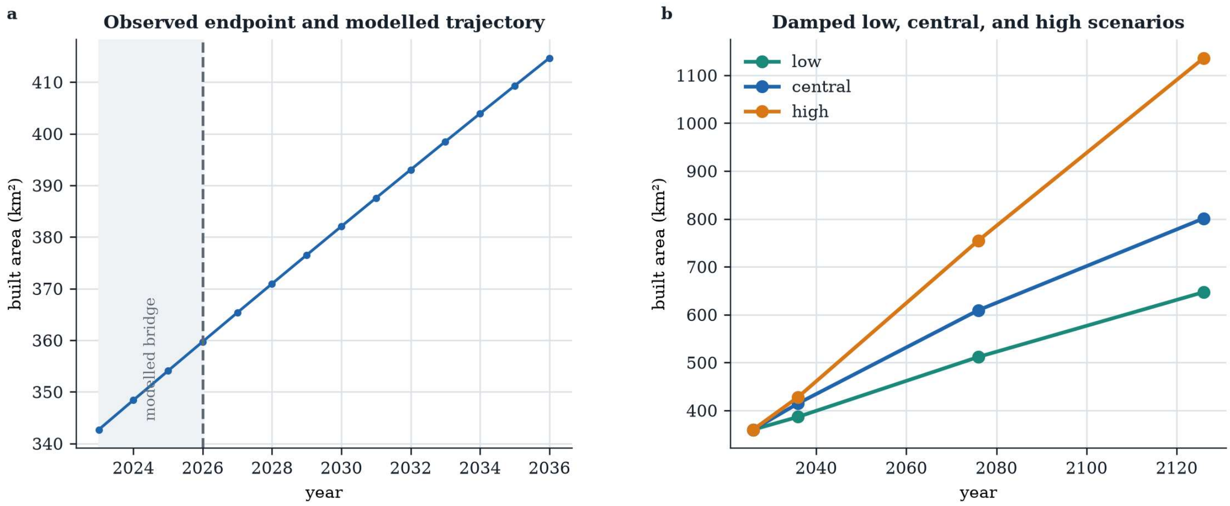

Figure 17. Demand trajectory. (a) Observed 2023 endpoint, modelled 2024–2026 bridge, and central near-term trajectory. (b) Low, central, and high built-area totals after damping. Lines between distant horizons aid reading and do not imply annual validation.

4.6 Land budget and spatial uncertainty

Central effective annual demand falls from 5.71 km² in the first step to 5.36 km² by 2036 and approximately 3.39 km² yr⁻¹ in the final five-year interval because remaining developable land declines. The land budget against which this is measured is R_0 = 1084.9 km², the effective developable area still available at the 2026 baseline after the terrain, flood and water factors of Equation 6 are applied and existing building is removed. It is a weighted area, not a count of vacant hectares, and it is smaller than the 1336.6 km² of effective developable land in the frame as a whole. By 2126 the low, central, and high scenarios consume 28.1%, 42.2%, and 73.1% of that budget. Only the high scenario approaches the point at which land availability, rather than demand, would govern the result.

All-run intersection over union among new-growth cells, as defined by Equation 17, is 0.12% at 2036, rising to 22.44% at 2076 and 37.51% at 2126. Read instead as the share of a single run's new area that all twelve runs share, the same three quantities are 0.42%, 43.68% and 65.44%. The underlying counts are 3,041 cells in the all-run intersection at 2036 against a 2,466,331-cell union, 1,165,173 against 5,192,637 at 2076, and 2,999,775 against 7,996,282 at 2126. Low near-term agreement is not an error in the arithmetic; it shows that a small required area can be distributed among many similarly weighted cells. Near-term maps should therefore be read as pressure corridors and neighbourhood envelopes, not field-by-field schedules (Figures 18 to 20). Section 4.4 gives the sharper version of the same warning: the model's skill is concentrated on perimeter thickening, so the parts of these maps that describe genuinely new districts are the parts it has least right to. These agreement figures are conditional on the selection temperature of Equation 15 and on the ensemble size. A sharper temperature should make replicates coincide more often than proportional sampling would, which suggests the figures are optimistic, but no sensitivity run has been performed and the direction is therefore an expectation rather than a result. The 0.12% should therefore not be read as an upper bound on near-term certainty: nothing reported here establishes that bound.

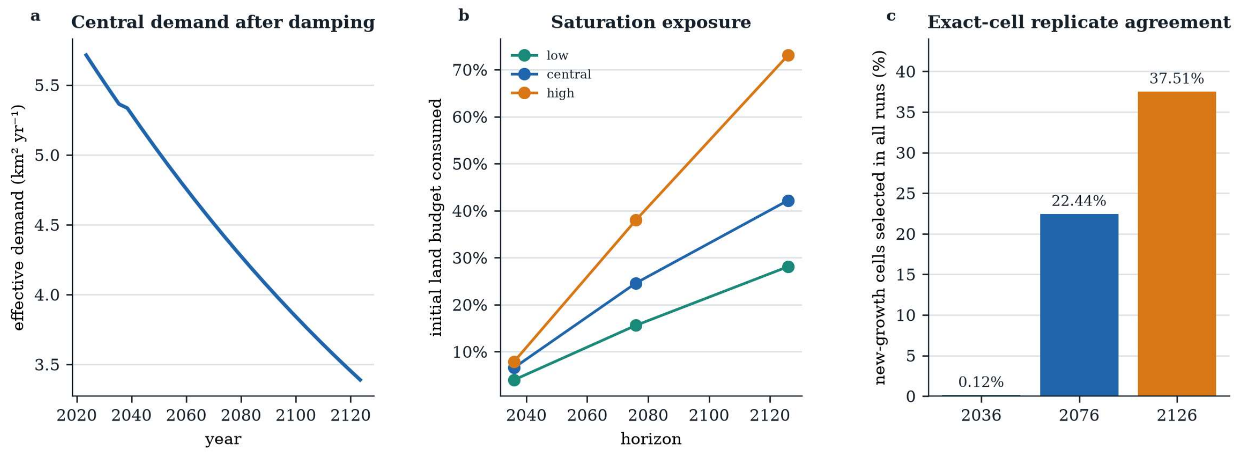

Figure 18. Demand damping and uncertainty. (a) Effective central demand. (b) Share of the initial effective land budget consumed. (c) Exact-cell agreement among the 12 replicates. The ensemble describes conditional allocation variability only; it does not include policy, economic, or demand-model uncertainty.

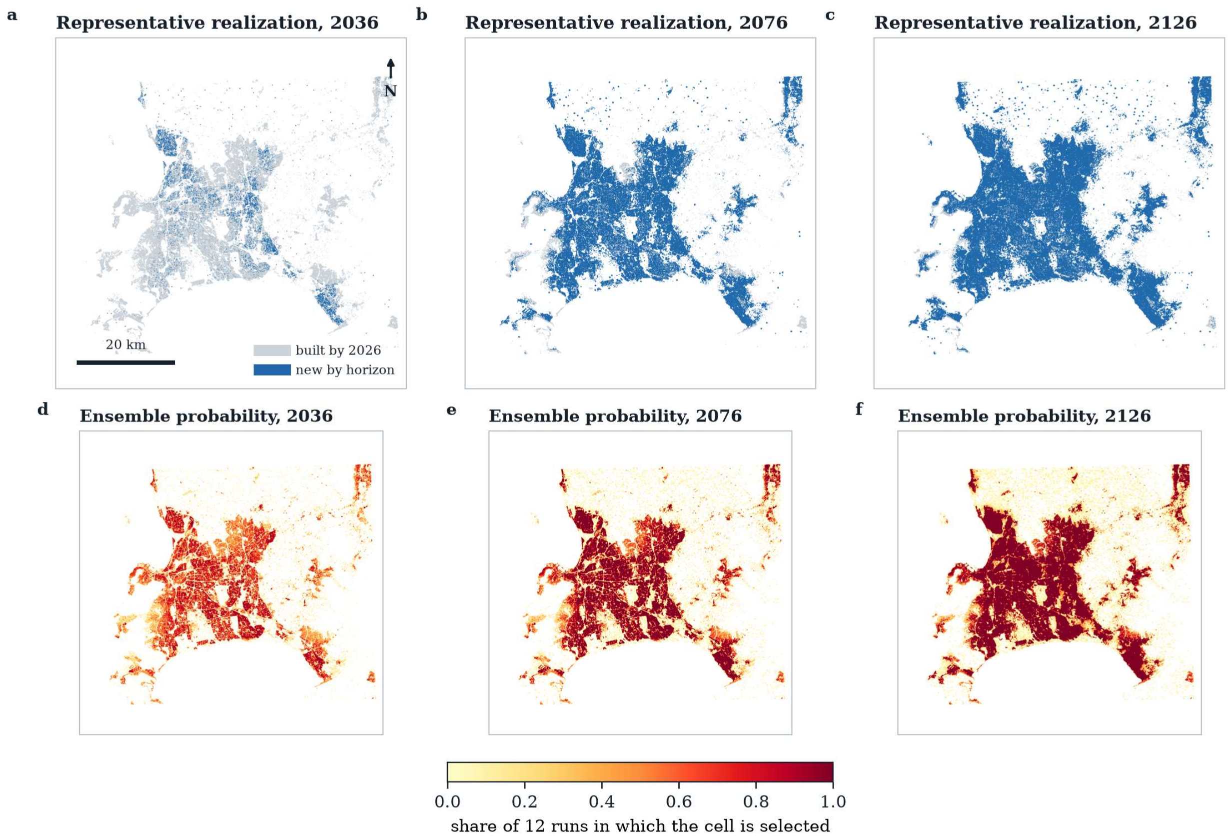

Figure 19. Central-scenario spatial outputs. Top row: one coherent representative realization at 2036, 2076, and 2126, with the 2026 baseline in grey and new selected cells in blue. Bottom row: ensemble probability, defined as the share of 12 runs selecting each cell. The 2126 output is an illustration of trend continuation, not a site-level prediction.

Figure 20 combines those horizons into a single map by colouring each cell with the earliest horizon at which it is selected. It is drawn from the archived realisation rasters, so the horizon boundaries and the areas are those of the run itself.

The isolated dots away from the built edge are worth naming, because they are a mechanism rather than noise. They are the detached-growth nuclei of Section 3.5: at every step a small share of demand is spent on new settlement seeds placed beyond 300 m of existing building, each grown as a compact patch. Most never receive a second allocation, because the adjacency and density terms of Section 3.3 score a lone seed in open country far below the built fringe, so they survive as isolated specks for the rest of the run. A few, placed near existing settlement or on high-developability land, are extended and become the small satellite clusters visible in panel (b). That asymmetry, many seeds and few survivors, is the model's only route to founding anything new, and Section 6.3 explains why it is also the assumption that grows most load-bearing over a century. Read at metropolitan scale it shows what the mode shares of Section 4.3 predict: the increments are not a clean advancing ring but a mixture of perimeter accretion, infill within the 2026 footprint, and a scatter of detached nuclei. The 2036 increment is barely visible, which is correct rather than a rendering fault, because 54.9 km² is under 4% of the 2026 baseline. In the north-eastern sector, where the fronts separate, the sequence is legible: growth runs along the existing corridors first, then thickens the small satellite settlements, and only then reaches open ground.

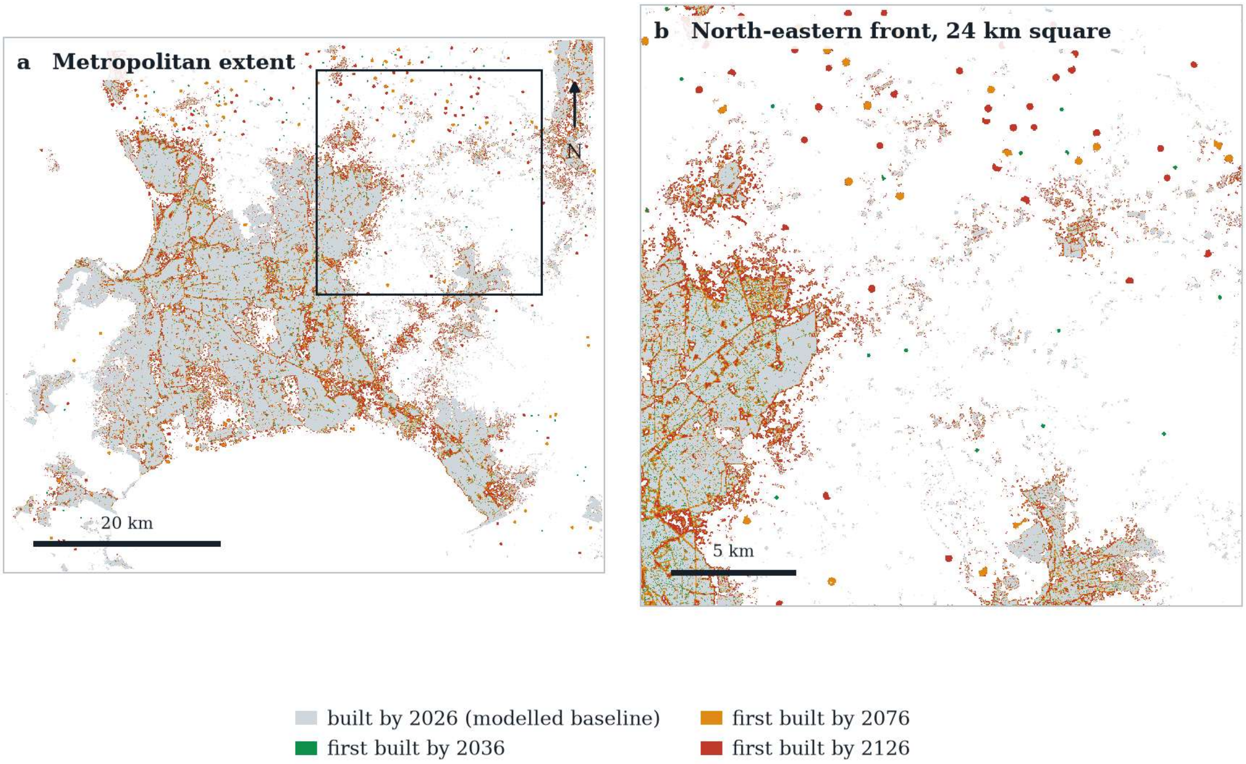

Figure 20. Central-scenario growth fronts, coloured by the earliest horizon at which each cell is selected in the representative realization. (a) Metropolitan extent at 50 m display blocks, with the extent of (b) marked. (b) A 24 km square on the north-eastern front at 20 m display blocks. Later horizons appear only where earlier ones have not already claimed the block, so the colours nest rather than overwrite. Isolated dots beyond the fringe are the detached-growth nuclei of Section 3.5, each a compact settlement seeded away from the built edge; most are never extended, which is why they persist as single dots rather than growing into blocks. Drawn from the archived realisation rasters, so the horizons and areas are those of the run itself.

4.7 The weight of terrain in the long run

The terrain constraint changes the hindcast score very little: removing it moves Figure of Merit from 16.97% to 16.52%. That is a fair measure over seven years, during which almost all growth occurred on land that was easy to build on in any case, and it is a misleading one for the long run. To separate the two, the allocator was run forward with and without the developability factor of Equation 6 until no eligible cell remained, five centuries of nominal model time. What the factor removes is the terrain and flood *render* surfaces of Section 3.2 and the water mask, not slope in degrees or flood depth in metres; the caveat of Section 2.2 travels with this experiment as it does with every other use of those inputs. This is a sensitivity experiment on the model, not a scenario for Cape Town, and no result in Sections 4.5 or 4.6 depends on it.

The two end states differ by far more than the hindcast suggests. With the constraint applied, 1,357 km² is taken and the unbuilt remainder is coherent: the Peninsula spine, the Hottentots Holland and Kogelberg ranges, the Cape Flats wetlands and the flood corridors survive as connected open land. With the constraint removed, 1,980 km² is taken. The two runs share 1,260 km²; 721 km² is taken only when terrain is ignored, and 97 km² only when it is applied, the latter because the constrained run concentrates the same nominal demand onto less land. The 721 km² is precisely the terrain the constraint protects, so the mountains fill in and the remaining gaps become the rounded voids left by an isotropic spreading process rather than anything with a physical cause. The comparison makes a general point about constraint layers in land-change models: a factor that barely moves a short-horizon score can dominate the long-horizon geometry, and short-horizon validation alone will not reveal it.

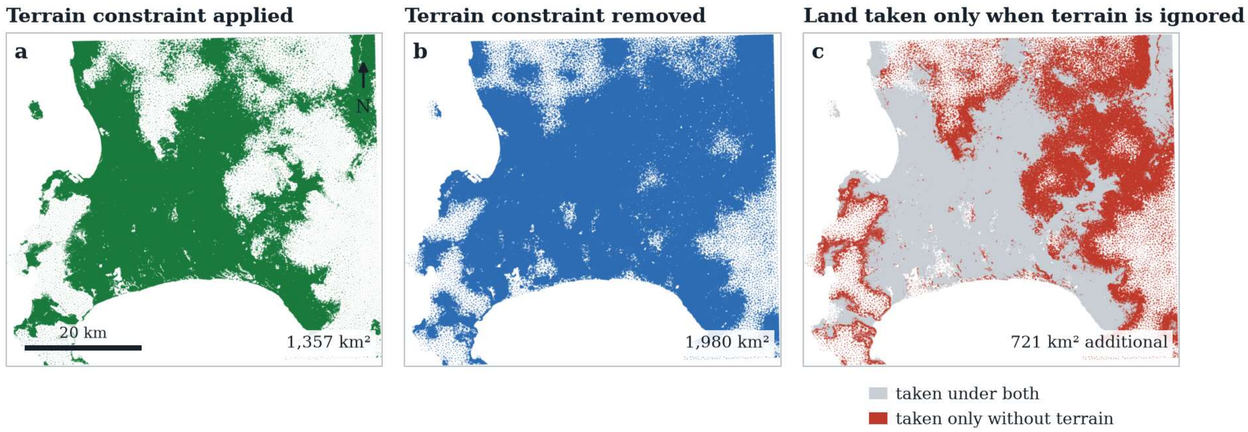

Figure 21. Saturation experiment. (a) Land taken when the allocator runs to saturation with the developability factor of Equation 6 applied. (b) The same run with the factor removed, so that the terrain and flood render surfaces and the water mask have no effect on allocation. (c) The difference, with the 1,260 km² taken under both runs in grey and the 721 km² taken only when terrain is ignored in red. The 97 km² taken only in the constrained run is not drawn separately. Areas printed on (a) and (b) are the totals for each run. This is a model sensitivity test carried far beyond any horizon for which the demand rules of Section 3.6 are meaningful; it is not a scenario. Its configuration and random seed were not archived with the production run, so it is reproducible in method but not bit-for-bit.

5. Downstream application: future ATM and branch screening

This section is a demonstration of what the forecast can and cannot support downstream, and it carries its own method and its own results because it is a separate model rather than a further result of the land-change model. It consumes the outputs of Sections 3 and 4 and returns nothing to them: no quantity below alters a single cell of the urban forecast. Every parameter introduced here is a declared judgement parameter, and none of them was fitted to any observed measure of banking demand, because no such measure was available to this study.

It is worth saying plainly what this section is not. Facility siting has a long formal literature, in which the p-median problem [18] and the maximal covering location problem [19] choose sites to optimise a stated objective over a demand surface and a distance metric. Nothing of that kind is attempted here. The demand surface is a forecast rather than an observation, no travel network or travel time enters the calculation, no objective function is optimised, and the output is a ranked list of neighbourhoods rather than a solved allocation. The comparison is offered so that a reader can place what follows, not to claim membership of that literature.

5.1 Aggregation and new-development pressure (method)

The service screen receives the 2026 built baseline, three ensemble probability rasters, and developability. Exact 16 × 16 blocks of 10 m cells are averaged to a 160 m grid; aggregated developability is written *D* with an overbar to distinguish it from the 10 m surface *D* of Equation 6. Zero is preserved as valid zero built fraction or zero probability even where raster metadata labels zero as NoData.

Let $Q_{i,h}$ be aggregated probability of being built by horizon *h* and $B_{i,2026}$ the aggregated baseline. New-development pressure is

$$N_{i,h} = max\left(Q_{i,h} - B_{i,2026},\ 0\right). \tag{19}$$

This subtraction stops already built, high-probability centres from being interpreted as new demand. It yields approximately 55 km² new pressure by 2036, 250 km² by 2076, and 442 km² by 2126 in the central scenario.

5.2 Catchment demand (method)

Both new pressure *N* and total future density *Q* are Gaussian-smoothed and divided by their 99th percentile. ATM smoothing uses 1.5 km; branch smoothing uses 4 km. With hats denoting robustly normalised surfaces,

$$Demand_{i,h}^{ATM} = 0.80\ \widehat{N}_{i,h} + 0.20\ \widehat{Q}_{i,h}, \tag{20}$$

$$Demand_{i,h}^{Branch} = 0.65\ \widehat{N}_{i,h} + 0.35\ \widehat{Q}_{i,h}. \tag{21}$$

These weights are declared judgement parameters. They were not fitted from customers, transactions, population, revenue, or travel behaviour.

5.3 Current-network gap (method)

Every 160 m cell receives straight-line distance *d* to the relevant facility tree. The ATM tree includes all 447 cash-access points; the branch tree includes 90 branches. A linear ramp converts distance to a bounded gap:

$$G(d;\ a,\ b) = clip\left((d - a)/(b - a),\ 0,\ 1\right). \tag{22}$$

For ATMs, a = 1 km and b = 5 km. For branches, a = 3 km and b = 15 km. Separate eligibility rules require at least 1 km from current cash access for an ATM candidate and 4 km from a current branch for a branch candidate. These distances are Euclidean and do not represent roads, travel time, pedestrian accessibility, or public transport.

5.4 Opportunity, shortlist, and screening results

Demand, gap, and a soft land factor are multiplied:

$$O_{i,h} = Demand_{i,h}\ G_i\ \left[0.35 + 0.65\ \sqrt{\left(\bar{D}_i\right)}\right]. \tag{23}$$

Cells are set to zero unless new-development pressure exceeds 0.0005, aggregated developability exceeds 0.02, and the minimum service distance is met. Let c_h denote the 99.5th percentile of the remaining opportunity values at horizon h. Scores are then scaled and clipped:

$$Score_{i,h} = 100 \; clip\left(O_{i,h} \; / \; c_h, \; 0, \; 1\right). \tag{24}$$

Scores are relative within one facility type and one horizon. An ATM score of 80 in 2036 is neither comparable with a branch score of 80 in 2126 nor an 80% probability of commercial success.

Candidates are sorted by score. The highest remaining cell is retained, then cells within 2.5 km of a selected ATM or 8 km of a selected branch are removed. Selection stops below score 25 or at 25 ATMs and 12 branches per horizon. The procedure returns 75 ATM and 36 branch candidates across the three horizons. Each point is the centre of a 160 m analysis cell, not a parcel.

Figure 22 sets out the same processing sequence as Sections 5.1 to 5.3 in a single static layout. Figure 23 reports the horizon surfaces.

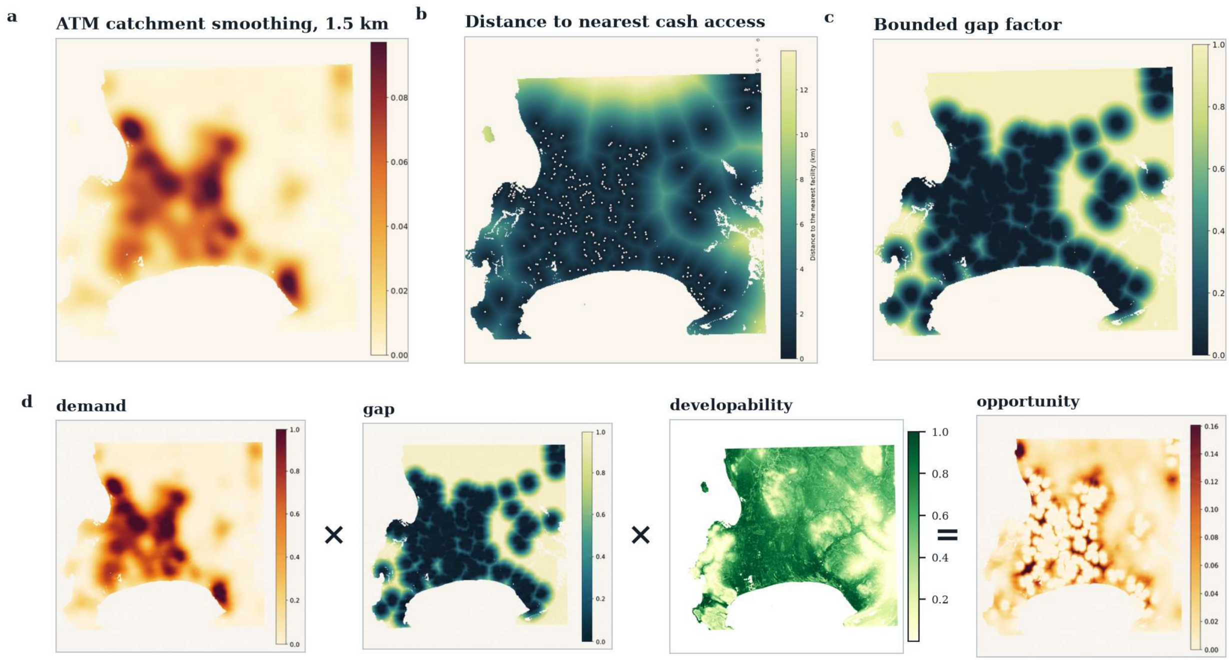

Figure 22. Service-network screening sequence, read top to bottom. (a) ATM and branch catchment smoothing at 1.5 km and 4 km. (b) Distance to the relevant existing service. (c) Distance converted to the bounded gap factor of Equation 22. (d) Multiplication of demand, gap, and land factor into opportunity, following Equation 23. The developability panel in row (d) is rendered from the production raster on a white canvas; the presentation version of this graphic drew it on a black satellite basemap. The calculation is downstream of, and does not alter, the urban forecast.

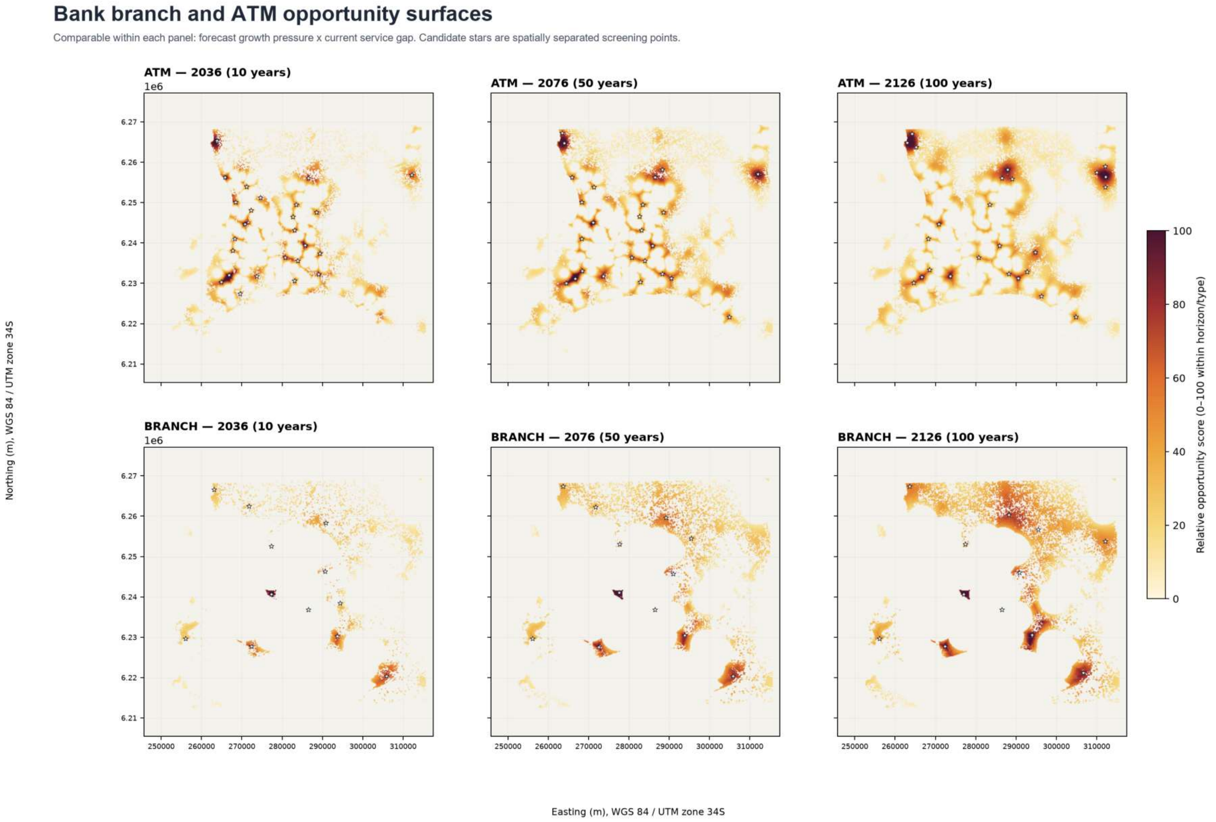

Figure 23. Relative ATM and branch opportunity surfaces for 2036, 2076, and 2126. Star symbols are spatially separated screening candidates. Colour is comparable only within one panel; blank areas fail demand, developability, distance, or score thresholds.

6. Discussion

6.1 What the framework contributes

The framework's main value is auditability. Observation cleaning is visible. Terrain and flood effects are not hidden inside the urban-pattern regression. Demand is not inferred from the same score that allocates location. Stochasticity produces an ensemble rather than one falsely precise map. The downstream service screen is mathematically and conceptually separate from the land-change model.

The blocked classifier diagnostic shows that the four urban-pattern predictors contain substantial ranking information, but the end-to-end hindcast is the more demanding result. Its 7.9-fold improvement over random allocation establishes non-random skill under an exact-cell metric, while the modest 16.97% FoM and morphology errors prevent overclaiming. This combination is more informative than either a high ROC-AUC without simulation or a visually plausible future map without a reconstruction test.

6.2 Demonstrated weaknesses

The largest demonstrated structural error is fringe growth. The model allocates 0.12% to fringe where 7.03% is observed. A future implementation should test an explicit fringe pool, patch-size distributions, intermediate-distance seed formation, or morphology-aware calibration. Infill is also overpredicted. This affects near-term interpretation because central forecast demand of 5.71 km² yr^{-1} is roughly 2.5 times lower than the 14.4 km² yr^{-1} the cleaned hindcast had to place, so the forecast never has to reach past the highest-scoring interior gaps in the way the hindcast did. Two design decisions work in the same direction and should be treated as candidates rather than as settled explanations: the selection temperature $\lambda = 0.35$, which sharpens allocation onto the highest-weight cells, and the 3 km candidate limit, which truncates the distance range in which fringe patches would form. Testing $\lambda = 1$ and a wider search radius against the same hindcast is the obvious next experiment, and it is cheap.

The second demonstrated error is directional. The simulated growth centroid moves 1.60 km on a bearing of 10.5° against an observed 2.21 km on 45.4°. A single global cosine multiplier is a blunt instrument for a city whose growth corridors are set by mountains, an airport, coastline and a specific post-apartheid settlement geography. A directionally varying or corridor-aware term, fitted per sector rather than globally, is a more promising direction than increasing the amplitude of the present one, which the sweep shows begins to cost Figure of Merit above 0.2.

The third weakness is the one the aggregate scores hide, and Section 4.4 measures it: skill is almost entirely confined to the first ring of cells beyond the existing built edge and to very small patches of change. This follows from the model's structure rather than from its calibration, since the adjacency term of Equation 8 and the candidate limit of Section 3.3 between them make the built edge the only place the main pool can readily reach, and the detached pool is deliberately small. Three consequences follow. A Figure of Merit computed over a period dominated by perimeter accretion, as 2016–2023 was, flatters the model relative to a period containing large single-event developments. Any application that depends on anticipating a new district, which includes most of the service screening in Section 5, is resting on the part of the model that performs worst. And the obvious remedies are structural rather than parametric: a patch-generating allocator that places contiguous blocks, a wider candidate radius, or an explicit process for one-step planned developments, none of which the present cell-by-cell design can express.

Six experiments would settle questions this paper can only pose, and none of them has been run. They are listed here so that the absence is explicit rather than implied. First, repeat the hindcast with the monotone projection of Section 3.3 disabled, and compare Figure of Merit, the four expansion-mode shares, and the two recall curves of Section 4.4. Second, repeat it at selection temperature $\lambda = 1$ and across a small sweep, and compare the same quantities plus replicate agreement. Third, replace the single unbuffered classifier split with a buffered, repeated spatial cross-validation, with the operating threshold chosen inside training. Fourth, reconcile the three centroid definitions of Section 3.5 and repeat the directional sweep under whichever is chosen. Fifth, vary the presence threshold τ of Section 3.1 across its plausible range and propagate the effect to the hindcast. Sixth, increase the ensemble beyond twelve replicates and check whether the probability surfaces, the agreement statistic and the service-screen shortlist are stable. The first two are cheap. The third and sixth are the most computationally expensive. None of them requires data this study does not already hold.

The exact principal hindcast raster was not saved with the production counts. The reconstructed visual mask differs by 638 hits and 0.05 FoM percentage points. The paper retains both the archived headline and the replay disclosure. A public release should preserve all seeds, draw order, environment information, and final rasters.

6.3 Limits of the future scenarios

The ensemble measures allocation variability conditional on one model, one constraint surface, one demand rule, and one selection temperature. It does not sample model form, calibration window, remote-sensing error, policy, zoning, land ownership, transport investment, migration, housing economics, infrastructure, water availability, climate adaptation, or technological change. The 2036 result is a near-term conditional scenario; 2076 is a strategic scenario; 2126 is an illustration of present-rule continuation. None is a parcel schedule.

One assumption deserves to be named separately because it grows more load-bearing the further the model runs. The detached-growth pool is fixed at the 2.8% share observed over 2016–2023 and is then held constant to 2126. Over the GHSL half-century, Cape Town's detached share was far higher, on the order of 37%, reflecting a period in which whole settlements were founded away from the existing edge. A century-scale projection that holds the recent, unusually low detached share constant will therefore tend to grow the existing city outward rather than to found new ones, and the 2126 map should be read with that in mind. Combined with the 3 km candidate limit, the model is structurally incapable of placing the kind of genuinely remote settlement that the region's own history contains. The 2126 result is best understood as the answer to a narrow question, namely what continuation of the recent pattern implies, rather than as a forecast of the settlement geography of the next century.

The modelled 2026 bridge is another source of uncertainty. A January 2026 satellite image supports visual audit, but no independent 2026 building mask is available for a pixel score. The bridge must remain labelled as model output.

6.4 Limits of the service screen

The ATM and branch demonstration omits population, customers, transactions, income, competitor networks, roads, travel time, public transport, pedestrian activity, safety, land ownership, zoning, planned developments, property availability, lease conditions, construction cost, and unit economics. Candidate points identify neighbourhoods for investigation, not sites to acquire or build. Long-horizon opportunity inherits all uncertainty in the underlying urban forecast and adds judgement-based catchment, demand, distance, and spacing parameters.

6.5 Transferability

The workflow can be recalibrated for other cities or services, but the Cape Town values are not portable defaults. Transfer requires a locally validated observation threshold, temporal cleaning audit, empirical constraint response, predictor bins and coefficients, directional structure, detached-growth mechanisms, demand scenarios, and service-distance rules. The scale of decision should also determine aggregation: the 160 m grid is appropriate for neighbourhood screening but not for parcel selection.

7. Conclusions

This study connects annual building evidence, explicit land constraints, dynamic urban-pattern ranking, independent demand scenarios, stochastic allocation, retrospective validation, and future service-network screening in one reproducible structure. The spatially blocked predictor diagnostic achieved ROC-AUC 0.880, while the complete quantity-matched hindcast achieved 29.02% hit rate and 16.97% FoM. The model reproduced dominant edge expansion but overpredicted infill, failed to reproduce most fringe growth, and recovered the observed direction of growth only partially.

Under the central conditional scenario, new built area after the modelled 2026 baseline is 54.9 km² by 2036, 249.7 km² by 2076, and 441.3 km² by 2126. Exact-cell agreement among replicates is extremely low at 2036, so the scientifically defensible unit of interpretation is a pressure corridor or neighbourhood, not an individual field. The downstream ATM and branch results further narrow this interpretation: they are ranked hypotheses where forecast pressure, present network gaps, and developable land coincide.

The principal safeguard is separation. Observation is not forecast; classifier diagnostic is not hindcast; placement validation is not demand validation; probability is not certainty; a neighbourhood screen is not a site recommendation; and a century continuation is not a prediction.

Acknowledgements

Public data providers are cited as sources and were not involved in the analysis, interpretation, or writing. No other person served as a collaborator or co-author.

Author contributions

Jaco Moolman: conceptualisation, methodology, software, validation, formal analysis, investigation, data curation, visualisation, writing, reviewing and editing the draft, and project administration.

Generative AI use

Generative AI assistance was used to inspect archived workflow documentation, support drafting and editing, recreate figures on paper-compatible backgrounds, assemble a code package, and check document layout. It was not treated as an author or source of scientific evidence. Numerical claims were traced to cited data products, archived run tables, or author-supplied code. The human author remains responsible for accuracy, citations, interpretation, rights, and submission.

Funding

The author received no specific funding for this work.

Competing interests

The author declares no competing interests.

Ethics statement

The study uses remote-sensing imagery, environmental rasters, model outputs, and facility-location data. It involves no human participants, identifiable personal data, animals, or clinical interventions. Institutional ethics approval and informed consent are not applicable.

Data and code availability

The public source products are cited below.

Code repository: https://github.com/JacoMoolman/cape-town-urban-expansion-forecast

The repository holds the forecast and network-screen code, configuration, figure-generation code, the method-to-code mapping, and the small derived evidence tables, under the PolyForm Noncommercial License 1.0.0. The parameters of the published run are recorded in `config/published_run.json`, copied verbatim from the run's own `summary.json`, and that file is authoritative. Two module defaults in the packaged code differ from it and are documented in `CONFIG_PROVENANCE.md`: the directional amplitude defaults to 0.4 where the run used the selected value of 0.20, and a docstring describes the selection temperature as 1.0 where the run used 0.35. A rerun starting from the module defaults would therefore not reproduce the published directional calibration unless the amplitude is set first. That licence covers the software only; third-party datasets and imagery retain their own terms. No archival DOI has been minted yet.

Reproducibility is partial and it is worth being exact about where. Nineteen of the twenty-three figures rebuild from the packaged evidence alone. Figure 15 rebuilds without its four imagery panels, which are Google Earth captures the author cannot redistribute. Figures 21 and 22 cannot be rebuilt at all, because the author-compiled facility snapshot is excluded pending a rights and sensitivity review; the package documents its required schema. Figure 8 is recomposited from a saved animation frame, because the underlying allocation-order array was not retained. Beyond the figures, the exact production hindcast raster was not saved and a replay is used in its place, the production coefficient curves were not archived separately from the fitted model object, and the five-century experiment of Section 4.7 has no archived configuration or seed. The scripts under `reference_workflows` carry absolute paths from the machine they were written on and will not run unchanged elsewhere. Everything the manuscript's headline numbers rest on, namely the archived run tables, the hindcast summary and the model statistics, is in the package. That is a narrower claim than saying every number in the paper can be traced through it, and the narrower claim is the correct one. The four close views in Figure 16(a)–(d) are Google Earth screen captures taken by the author, reproduced with attribution under Google's geo guidelines for illustrative use. They are the only figure content in this paper not generated from the archived evidence, they are not redistributed in the code package, and the argument they illustrate is carried quantitatively by panels (e) and (f) without them.

References

[1] Sirko, W., Brempong, E. A., Marcos, J. T. C., Annkah, A., Korme, A., Hassen, M. A., Sapkota, K., Shekel, T., Diack, A., Nevo, S., Hickey, J., & Quinn, J. A. (2023). High-resolution building and road detection from Sentinel-2. *arXiv*. https://doi.org/10.48550/arXiv.2310.11622

[2] Pesaresi, M., & Politis, P. (2023). GHS-BUILT-S R2023A: GHS built-up surface grid, derived from Sentinel-2 composite and Landsat, multitemporal 1975–2030. European Commission, Joint Research Centre. https://doi.org/10.2905/9F06F36F-4B11-47EC-ABB0-4F8B7B1D72EA

[3] Pekel, J.-F., Cottam, A., Gorelick, N., & Belward, A. S. (2016). High-resolution mapping of global surface water and its long-term changes. *Nature, 540*, 418–422. https://doi.org/10.1038/nature20584

[4] Copernicus Programme. (2024). Copernicus DEM GLO-30, 2024 release. Digital surface model at 30 m resolution, Earth Engine catalogue entry COPERNICUS/DEM/GLO30_2024_1. https://developers.google.com/earth-engine/datasets/catalog/COPERNICUS_DEM_GLO30_2024_1

[5] Baugh, C. A., Colonese, J., D'Angelo, C., Dottori, F., Neal, J. C., Prudhomme, C., Salamon, P., & Trigg, M. A. (2024). Global river flood hazard maps, version 2.1. European Commission, Joint Research Centre, Copernicus Emergency Management Service. https://developers.google.com/earth-engine/datasets/catalog/JRC_CEMS_GLOFAS_FloodHazard_v2_1

[6] Yamazaki, D., Ikeshima, D., Sosa, J., Bates, P. D., Allen, G. H., & Pavelsky, T. M. (2019). MERIT Hydro: A high-resolution global hydrography map based on latest topography dataset. *Water Resources Research, 55*, 5053–5073. https://doi.org/10.1029/2019WR024873

[7] White, R., & Engelen, G. (1993). Cellular automata and fractal urban form: A cellular modelling approach to the evolution of urban land-use patterns. *Environment and Planning A, 25*(8), 1175–1199. https://doi.org/10.1068/a251175

[8] Clarke, K. C., Hoppen, S., & Gaydos, L. (1997). A self-modifying cellular automaton model of historical urbanization in the San Francisco Bay area. *Environment and Planning B: Planning and Design, 24*(2), 247–261. https://doi.org/10.1068/b240247

[9] Verburg, P. H., Schot, P. P., Dijst, M. J., & Veldkamp, A. (2004). Land use change modelling: Current practice and research priorities. *GeoJournal, 61*(4), 309–324. https://doi.org/10.1007/s10708-004-4946-y

[10] Liang, X., Guan, Q., Clarke, K. C., Liu, S., Wang, B., & Yao, Y. (2021). Understanding the drivers of sustainable land expansion using a patch-generating land use simulation (PLUS) model: A case study in Wuhan, China. *Computers, Environment and Urban Systems, 85*, 101569. https://doi.org/10.1016/j.compenvurbsys.2020.101569

[11] van Vliet, J., Bregt, A. K., Brown, D. G., van Delden, H., Heckbert, S., & Verburg, P. H. (2016). A review of current calibration and validation practices in land-change modeling. *Environmental Modelling & Software, 82*, 174–182. https://doi.org/10.1016/j.envsoft.2016.04.017

[12] Pontius, R. G., Boersma, W., Castella, J.-C., Clarke, K., de Nijs, T., Dietzel, C., Duan, Z., Fotsing, E., Goldstein, N., Kok, K., Koomen, E., Lippitt, C. D., McConnell, W., Mohd Sood, A., Pijanowski, B., Pithadia, S., Sweeney, S., Trung, T. N., Veldkamp, A. T., & Verburg, P. H. (2008). Comparing the input, output, and validation maps for several models of land change. *The Annals of Regional Science, 42*, 11–37. https://doi.org/10.1007/s00168-007-0138-2

[13] Pontius, R. G., & Millones, M. (2011). Death to Kappa: Birth of quantity disagreement and allocation disagreement for accuracy assessment. *International Journal of Remote Sensing, 32*(15), 4407–4429. https://doi.org/10.1080/01431161.2011.552923

[14] Roberts, D. R., Bahn, V., Ciuti, S., Boyce, M. S., Elith, J., Guillera-Arroita, G., Hauenstein, S., Lahoz-Monfort, J. J., Schröder, B., Thuiller, W., Warton, D. I., Wintle, B. A., Hartig, F., & Dormann, C. F. (2017). Cross-validation strategies for data with temporal, spatial, hierarchical, or phylogenetic structure. *Ecography, 40*(8), 913–929. https://doi.org/10.1111/ecog.02881

[15] Robertson, T., Wright, F. T., & Dykstra, R. L. (1988). *Order restricted statistical inference*. Wiley.

[16] Google Research. (2024). Open Buildings 2.5D Temporal, version 1. Earth Engine catalogue entry GOOGLE/Research/open-buildings-temporal/v1. https://developers.google.com/earth-engine/datasets/catalog/GOOGLE_Research_open-buildings-temporal_v1

[17] Kool, W., van Hoof, H., & Welling, M. (2019). Stochastic beams and where to find them: The Gumbel-top-k trick for sampling sequences without replacement. *Proceedings of Machine Learning Research, 97*, 3499–3508. https://proceedings.mlr.press/v97/kool19a.html

[18] Hakimi, S. L. (1964). Optimum locations of switching centers and the absolute centers and medians of a graph. *Operations Research, 12*(3), 450–459.

[19] Church, R., & ReVelle, C. (1974). The maximal covering location problem. *Papers of the Regional Science Association, 32*, 101–118.